

EVANESCENT WAVEGUIDE MODES IN SUBWAVELENGTH HOLE
ARRAYS AND THEIR ROLE IN ENHANCING THE PERFORMANCE
OF QUANTUM DOT INFRARED PHOTODETECTORS

BY

RUNYU LIU

ABSTRACT OF A THESIS SUBMITTED TO THE FACULTY OF THE
DEPARTMENT OF ELECTRICAL AND COMPUTER ENGINEERING
IN PARTIAL FULFILLMENT OF THE REQUIREMENTS
FOR THE DEGREE OF
MASTER OF SCIENCE
UNIVERSITY OF MASSACHUSETTS LOWELL
2011

Thesis Supervisor: Xuejun Lu, Ph.D.,

Associate Professor, Department of Electrical and Computer Engineering

UMI Number: 1507740

All rights reserved

INFORMATION TO ALL USERS

The quality of this reproduction is dependent upon the quality of the copy submitted.

In the unlikely event that the author did not send a complete manuscript and there are missing pages, these will be noted. Also, if material had to be removed, a note will indicate the deletion.



UMI 1507740

Copyright 2012 by ProQuest LLC.

All rights reserved. This edition of the work is protected against unauthorized copying under Title 17, United States Code.



ProQuest LLC
789 East Eisenhower Parkway
P.O. Box 1346
Ann Arbor, MI 48106-1346

EVANESCENT WAVEGUIDE MODES IN SUBWAVELLENGTH HOLE
ARRAYS AND THEIR ROLE IN ENHANCING THE PERFORMANCE OF
QUANTUM DOT INFRARED PHOTODETECTORS

BY

RUNYU LIU

UNIVERSITY OF MASSACHUSETTS LOWELL (2011)

SUBMITTED IN PARTIAL FULFILLMENT OF THE REQUIREMENTS
FOR THE DEGREE OF MASTER OF SCIENCE
DEPARTMENT OF ELECTRICAL AND COMPUTER ENGINEERING
UNIVERSITY OF MASSACHUSETTS LOWELL

Signature of:

Author: Runyu Liu Date: 12/02/2011
Runyu Liu

Supervisor: Xuejun Lu

Committee Member: Tingshu Hu

Committee Member Joel Therrien

ABSTRACT

Accumulated strain existing in multi-stacked Quantum Dot layers has been a major issue for the Quantum Dot Infrared Photodetectors (QDIPs), which limits the number of layers that can be grown for the device. This inherent character leads to a thin active region which is only able to interact with a small percentage of infrared energy inside the detector. In this thesis, a metallic two dimensional subwavelength hole array was integrated on the QDIPs; photocurrent enhancement of the QDIPs was observed at different plasmonic resonance wavelengths; enhancement ratio and its dependence on the hole diameter was investigated; evanescent waveguide mode and its impact on near field transmission was analyzed by changing the dimension of the hole. Finally, the performance (photocurrent, responsivity, detectivity) improvement was observed and reported.

ACKNOWLEDGMENT

First of all, I would like to thank my parents, it's their endless love and understanding that enable me to enjoy every moment in my life, overcome difficulties, confront fear, chasing dreams; without them, I have no idea whether I can come this far.

Two and a half years may not be a long time compared to a person's whole life, but I should say the time I spend in my group will have a great influence for my life, during this time, I have learned a lot from my advisor, Prof. Xuejun Lu. He set a good example for me, both in study and in life, his enthusiasm in work, sense of responsibility for family and understanding to his students gave me great inspiration to study, to work and to love. The greatness help and support from him will be the most valuable treasure in my life.

I would like to thank Prof. Tingshu Hu, Prof. Joel Therrien, for their time and effort to review my thesis. Their useful comments are great.

TABLE OF CONSTANTS

I.	INTRODUCTION	1
1.1	Photodetectors	1
1.1.1	Types of photodetectors	2
1.1.2	Quantum Dot Infrared Photodetector.....	5
1.2	Plasmonic Enhanced Transmission.....	17
1.2.1	What is a Surface Plasmon Polariton.....	17
1.2.2	Derivation of SPP.....	19
1.2.3	Excitation of Surface Plasmon Polaritons.....	25
1.2.4	Extraordinary Optical Transmission 2DMHA	29
II.	GROWTH, FABRICATION AND TEST.....	32
2.1	Growth	32
2.1.1	Growth Technology (MBE)	32
2.1.2	Growth Condition and Process	32
2.2	Fabrication	33
2.3	Test Setup.....	35
2.3.1	Spectral Response Measurement of QDIPs	35
2.3.2	Photocurrent Measurement of QDIPs	38
2.3.3	Dark Current and Noise Current Measurement of QDIPs	40
III.	SPP ENHANCED QDIP	43

3.1	Transmission Properties of 2D Metal Hole Arrays on GaAs.....	44
3.1.1	Excited by Periodic Hole Arrays	44
3.1.2	Wavelength Selection---Lattice Constant Variation.....	45
3.1.3	Doping Effect---Dielectric Constant Variation.....	46
3.1.4	Filling Factor Effect---Hole Size Variation	49
3.2	Surface Plasmon Enhanced QDIPs	52
3.2.1	Integration of 2DMHA on QDIPs and the Photocurrent Enhancement.	
	52
3.2.2	Enhancement Peak Shifting and Its Dependence on Lattice Constant ..	
	56
3.2.3	Enhancement Ratio Variation and Its Dependence on Filling Factor	59
3.2.4	Performance Enhancement for Different Filling Factors.....	72
IV.	CONCLUSION AND FUTURE WORK	77
4.1	Conclusion	77
4.2	Future Work	78
V.	LITERATURE CITED.....	81

LIST OF TABLES

	Page
Table 3. 1 Enhancement peak and ratio with different lattice constant.....	58
Table 3. 2 First few roots for differential of first Bessel Function	64
Table 3. 3 Relationship between d and kz in air.....	65
Table 3. 4 Relationship between d and kz in GaAs.....	67

LIST OF ILLUSTRATIONS

	Page
Figure 1. 1 Photodetecting process	1
Figure 1. 2 Photoconductor.....	2
Figure 1. 3 reverse-biased photodiode.....	3
Figure 1. 4 minority carrier distribution before light incident in.....	4
Figure 1. 5 Photoemissive detector.....	5
Figure 1. 6 A Quantum Well made by GaAs and AlGaAs.....	7
Figure 1. 7 Dispersion curve of k of a quantum well in x and y direction	8
Figure 1. 8 Density of State for Bulk, Quantum Well and Quantum Dot.	10
Figure 1. 9 Schematic view (3D) of light incident on a quantum well with different angle	11
Figure 1. 10 Schematic view of light incident on a quantum well with different angle....	12
Figure 1. 11 Lateral confinement in a pyramid-like quantum dot.....	13
Figure 1. 12 Electron gas movement under the E-Field	18
Figure 1. 13 The E-field oscillation at the interface between a metal and a dielectric.....	19
Figure 1. 14 Dispersion relation of SPPs at the interface between metal and air.....	25
Figure 1. 15 Prism coupling to SPPs through attenuated total internal reflection in the Kretschmann (a) and Otto (b) configuration.	27
Figure 1. 16 Light diffracted by a grating.....	27
Figure 1. 17 Wave vector conservation	28
Figure 1. 18 the excitation of SPP by gratings	29

Figure 2. 1 QDIP fabrication	34
Figure 2. 2the schematic view of FTIR spectrometer.....	36
Figure 2. 3 The schematic diagram of spectral response testing setup for QDIPs.	37
Figure 2. 4 Black body radiations at different temperature.	38
Figure 2. 5 Photocurrent test set up in CMOS lab.....	39
Figure 2. 6 Photocurrent tested on sample UML0285.....	39
Figure 2. 7 Dark current of QDIPs measured by source meter.	40
Figure 2. 8 The schematic view of noise current setup.	41
Figure 2. 9 Dark current spectrum under different bias voltage.....	41
Figure 3. 1 Dispersion relationship of SPP and photon.....	44
Figure 3. 2 2D hole array perforated on Au film, period 2.8um, hole size 1.4um.	45
Figure 3. 3 Transmission profile of the 2D Metal Hole Array.	46
Figure 3. 4 transmission profile of 2D metal hole array on GaAs with different doping level.....	48
Figure 3. 5 transmission profile of 2D metal hole arrays with different hole size.	49
Figure 3. 6 The relationship between Peak Value and hole size.	50
Figure 3. 7 The relationship between FWHM and hole size.	51
Figure 3. 8 The relationship between Q factor and hole size.	51
Figure 3. 9 Comparison between standard QDIP and SP integrated QDIP.....	52
Figure 3. 10 FTIR response of regular QDIP and Plasmonic integrated QDIP with period 2.6um.	53
Figure 3. 11 Enhancement Ratio for 2.6 μ m period 2DMHA on UML0285.	54

Figure 3. 12 Photocurrent Enhancement for 2.6 μ m period 2DMHA on UML0285.....	54
Figure 3. 13 Gain Enhancement for 2.6 μ m period 2DMHA on UML0285.....	55
Figure 3. 14 Responsivity Enhancement for 2.6 μ m period 2DMHA on UML0285.....	55
Figure 3. 15 Detectivity Enhancement for 2.6 μ m period 2DMHA on UML0285.....	56
Figure 3. 16 Quantum Efficiency Enhancement for 2.6 μ m period 2DMHA on UML0285.	
.....	56
Figure 3. 17 FTIR and Photocurrent enhancement for period 2.4 μ m.	57
Figure 3. 18 FTIR and Photocurrent enhancement for period 2.8 μ m.	58
Figure 3. 19 FTIR and Photocurrent enhancement for period 3.0 μ m.	58
Figure 3. 20 Regular QDIPs integrated with 2DMHA of different filling factor 20X.....	59
Figure 3. 21Regular QDIPs integrated with 2DMHA of different filling factor 50X.....	60
Figure 3. 22 Transmission of SP on GaAs Period 2.8um.....	60
Figure 3. 23 FTIR spectral response of the mesa integrated with 2DMHA of different filling factors.....	61
Figure 3. 24 Cylindrical waveguide in the metal film.....	62
Figure 3. 25 E-field decay of different hole diameters in the air hole.....	65
Figure 3. 26 Decay curve on the QDIP.....	66
Figure 3. 27 FWHM widths different hole diameters.....	67
Figure 3. 28 E-field distribution inside of GaAs.	68
Figure 3. 29 Percentage of E occupied by QDs layer through different hole diameters. ..	68
Figure 3. 30 Matlab calculation for 2.6 series on 10 layer QDs.....	69
Figure 3. 31 FTIR response of 1.1 μ m, 1.2 μ m and 1.3 μ m on UML0287.	70
Figure 3. 32 FTIR response of 1.4 μ m and 1.5 μ m on UML0287.	70

Figure 3. 33 Matlab calculation for 2.8 series on 20 layer QDs.....	71
Figure 3. 34 FTIR response of 1.2 μm -1.8 μm on UML2461.....	71
Figure 3. 35 Photocurrent of UML0287 with different filling factors (bare&1.1um-1.3um).....	72
Figure 3. 36 Photocurrent of UML0287 with different filling factors (bare&1.4um, 1.5um).....	73
Figure 3. 37 Responsivity of UML0287 with different filling factors (bare&1.1um-1.3um).....	73
Figure 3. 38 Responsivity of UML0287 with different filling factors (bare&1.4um, 1.5um).....	74
Figure 3. 39 Detectivity of UML0287 with different filling factors (bare&1.1um-1.3um).	74
Figure 3. 40 Detectivity of UML0287 with different filling factors (bare&1.4um, 1.5um).	74
Figure 3. 41 Photocurrent enhancement on UML2461 with different filling factors.....	75
Figure 3. 42 Responsivity enhancement on UML2461 with different filling factors.	75
Figure 3. 43 Detectivity enhancement on UML2461 with different filling factors.....	76

I. INTRODUCTION

1.1 Photodetectors

A photodetector is a specific semiconductor device which is capable of detecting the existence of incident photons [1]. Different from thermal detector that mainly responds to the heating effect of the optical radiation, photodetector is able to sensing the light by direct interaction between the optical energy and the semiconductor material.

The underlying principle of a photodetector is converting the optical signal into electrical signal. Under the radiation of an optical field, excess carriers are generated from the active region in the semiconductor, the electrons in conduction band and the holes in valence band [2]. The increase of electron-hole pairs is bonding to the variation of the physical parameters. By analyzing the physical parameters through associated circuitry or systems, the characteristic of the incident photons can be identified.

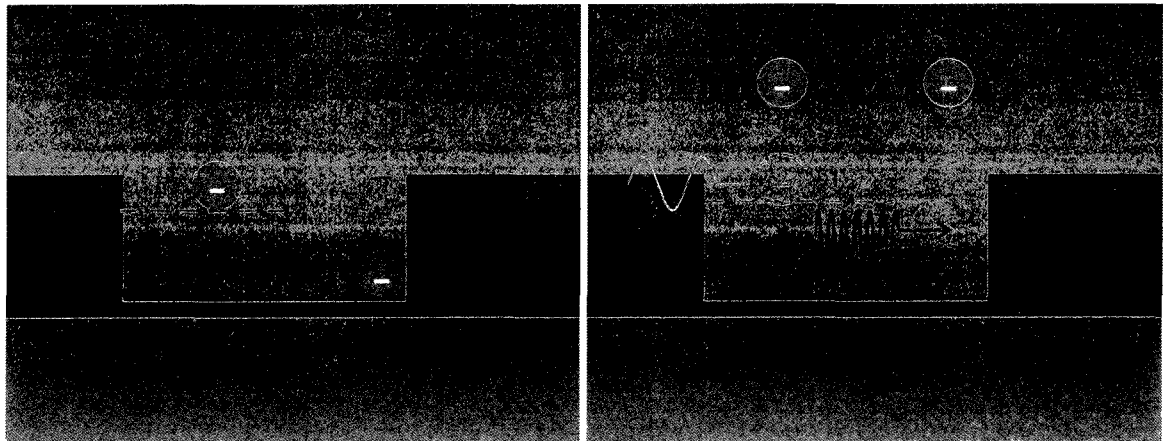


Figure 1.1 Photodetecting process

Figure 1.1 illustrates the working mechanism for the photodetecting process. Before the photon flux incident on the material, the electrons in the p-n junction cannot make any contribution to the electric current, either because that they were blocked by

the potential barrier (a), or is trapped by a bound state (b). Only if the electron was excited by the photons with enough energy, it is possible to generate a current that flow through the device.

1.1.1 Types of photodetectors

According to the operating mechanisms, photodetectors can be mainly classified as three different types, the Photoconductors, Photovoltaic detectors and Photoemissive detectors [1].

1.1.1.1 Photoconductors

Basically, a Photoconductor is an optical-sensitive element, which can response to the light through changing its resistance or conductance. Figure 1.2 shows the geometry of a photoconductor.

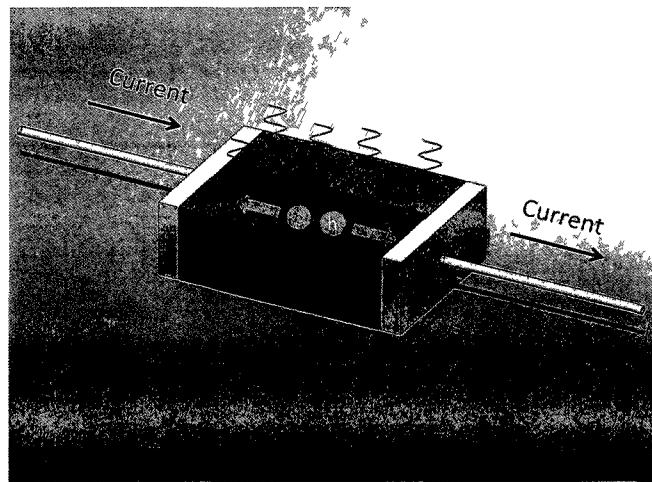


Figure 1. 2 Photoconductor

Originally, the conductivity at thermal-equilibrium state is [2]:

$$\sigma_0 = e(\mu_n n_0 + \mu_p p_0) \quad (1.1)$$

Once the material absorbed the photon energy, excess carriers are generated inside the device, consequently, the conductivity increase to:

$$\sigma = e[\mu_n(n_0 + \delta n) + \mu_p(p_0 + \delta p)] \quad (1.2)$$

where δn and δp are corresponding to the excess electrons and holes respectively.

Compared with the initiate state, conductivity increases by the mount of:

$$\Delta\sigma = e(\delta p)(\mu_n + \mu_p) \quad (1.3)$$

1.1.1.2 Photovoltaic detector

A photovoltaic detector also called photodiode. Utilizing the rectifying characteristic of a p-n junction, a photodiode can produce a voltage or current response to the optical radiation under a reverse bias [2].

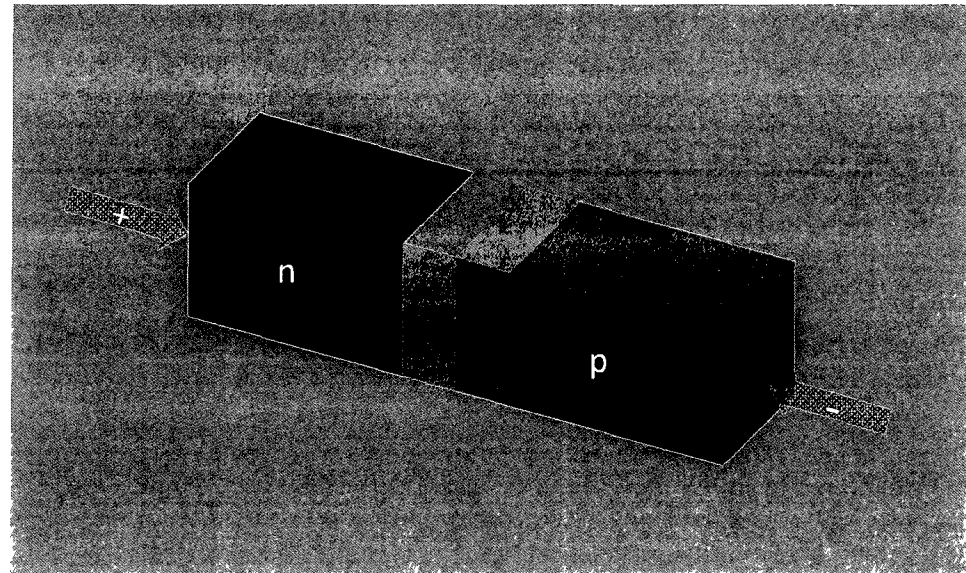


Figure 1. 3 reverse-biased photodiode

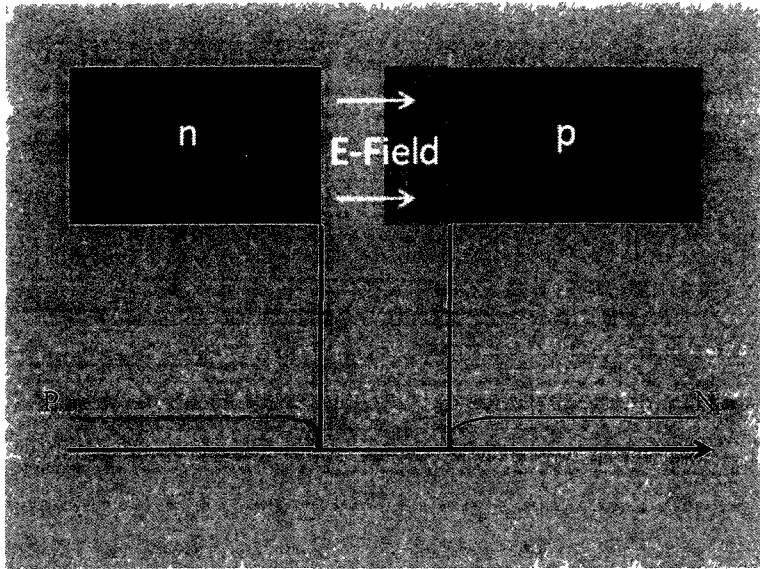


Figure 1. 4 minority carrier distribution before light incident in Figure 1.3 shows the reverse-biased diode and Figure 1.4 shows the minority carrier distribution in the reverse-biased junction prior to light illumination.

Photons enter from the top surface and pass through the p-type material (thin enough, the absorption can be neglect), absorbed in the space charge region then give rise to the electron-hole pairs. Immediately, the excess carriers generated by the light-matter interaction were swept out of the depletion region, electrons were drifted to n region, while holes flow toward p region. Photocurrent density can be described as blow [1]:

$$J_{L1} = e \int G_L dx \quad (1.4)$$

1.1.1.3 Photoemissive detector

Unlike the photovoltaic and photoconductor detectors, the photoemissive detectors can work with an external photoelectron emission, which means that the photo-generated current is no longer flowing inside the device, but move in the external field. An energetic electron is capable to overcome the work function of the material, as long as

it gets sufficient kinetic energy from the photon. Once it jumps out of the surface and travels in the vacuum, the external electric field will pull it to the electrode, therefore, counted as an increase of the current. Figure 1.5 [1] shows the working process of a photoemissive detector.

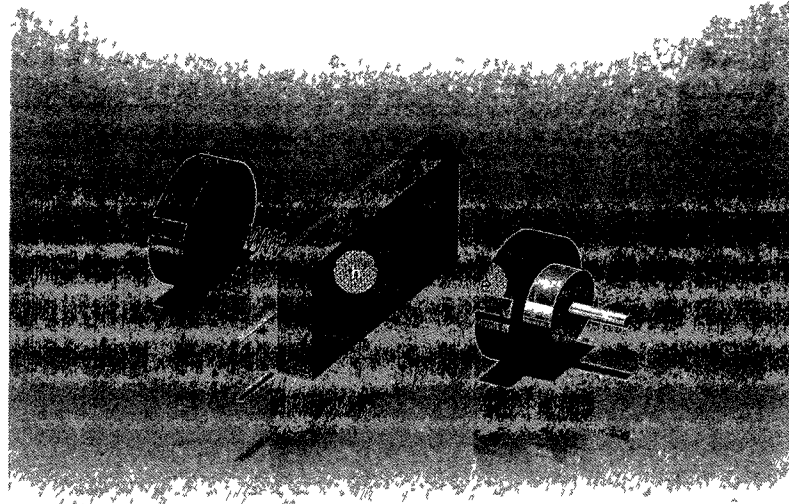


Figure 1. 5 Photoemissive detector

1.1.2 Quantum Dot Infrared Photodetector

Infrared sensing and detecting technology has been widely used in both military and civil constructions [3], including night version, missile tracking and environmental monitoring. As monochromatic light moves further to the infrared region, traditional Interband Transition Photodetector fails to response the optical signal. The reason why it becomes transparent to the infrared light is that, photodetectors can only response to the photons with energy equal or larger than the bandgap of the materials, when it comes to the infrared, photon energy is insufficient to excite an electron jumping over the bandgap. To match the special energy requirement, it is necessary to build up a bandgap engineered photodetector.

Quantum Dot Infrared Photodetector (QDIPs) is a well-developed semiconductor device. Due to the 3D quantum confinement of the Quantum Dot (QD) [4], QDIPs possess several prominent characteristics, such as capability of detection normal incident light [3]; reduced dependence of the carrier distribution on the temperature; higher photoconductive gain; carrier lifetimes 10-100 times longer than QWIPs, giving rise to lower dark current, all the advantages make it surpass Quantum Well Infrared Photodetectors (QWIPs) [5].

1.1.2.1 Properties of a QD

The most important characteristic of a quantum dot (QD) proved to be its three dimensional confinement of the carriers [3]. Compared with a quantum well, the additional two confinements removes the rest degrees of freedom for the carrier, hence introduces some interesting properties of the QD. For simplicity, let's start with the quantum well then move on to a quantum box.

Three dimensional confinement

A one dimensional confinement has been applied in z direction, as illustrated by Figure 1.6.

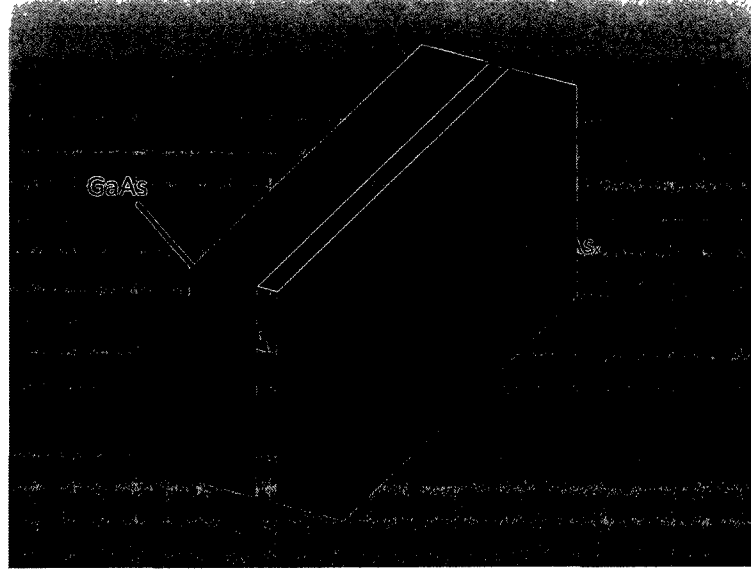


Figure 1. 6 A Quantum Well made by GaAs and AlGaAs

Therefore, the schrodinger equation can be derived as [6]: \hbar

$$-\frac{\hbar^2}{2m} \left(\frac{\partial^2}{\partial x^2} + \frac{\partial^2}{\partial y^2} + \frac{\partial^2}{\partial z^2} \right) \varphi + V(z)\varphi = E\varphi \quad (1.1)$$

the eigen function can be written as:

$$\varphi(x, y, z) = \varphi_x(x)\varphi_y(y)\varphi_z(z) \quad (1.2)$$

Substitute $\varphi(x, y, z)$ into (1.1), then we obtained:

$$-\frac{\hbar^2}{2m} \frac{\partial^2 \varphi_x}{\partial x^2} = E_x \varphi_x \quad (1.3a)$$

$$-\frac{\hbar^2}{2m} \frac{\partial^2 \varphi_y}{\partial y^2} = E_y \varphi_y \quad (1.3b)$$

$$-\frac{\hbar^2}{2m} \frac{\partial^2 \varphi_z}{\partial z^2} + V(z)\varphi_z = E_z \varphi_z \quad (1.3c)$$

For (1.3a) and (1.3b), there is no confinement in x and y direction, see Figure 1.7.

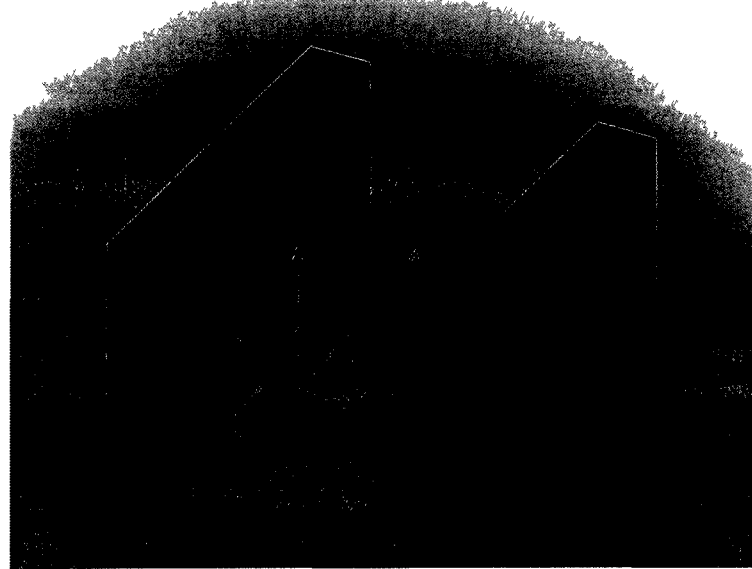


Figure 1. 7 Dispersion curve of k of a quantum well in x and y direction

so the eigen function should be in the form of a traveling wave, like: $\exp(i k_x x)$,
 $\exp(i k_y y)$, thus:

$$-\frac{\hbar^2}{2m} \frac{\partial^2}{\partial x^2} \exp(i k_x x) = E_x \exp(i k_x x) \quad (1.4)$$

$$\frac{\hbar^2 k_x^2}{2m} = E_x \quad (1.5)$$

And the solution for the one dimensional confined axis is

$$E_z = E_n = \frac{\hbar^2 \pi^2 n^2}{2m L_z^2} \quad (1.6)$$

Totally, the energy within a quantum well is [6]:

$$E = E_n + \frac{\hbar^2 k_x^2}{2m} + \frac{\hbar^2 k_y^2}{2m} \quad (1.7)$$

When it comes to a quantum box with dimensions L_x , L_y and L_z , the wave function and energy states will change respectively, for the conduction band:

$$\varphi_{n,l,m} = \left(\frac{2}{L}\right)^{3/2} \sin\left(\frac{n\pi}{L_x}x\right) \sin\left(\frac{n\pi}{L_y}y\right) \sin\left(\frac{n\pi}{L_z}z\right) \quad (1.8)$$

$$E = E_c + \frac{\hbar^2\pi^2}{2m_c^*L_x^2} n^2 + \frac{\hbar^2\pi^2}{2m_c^*L_y^2} l^2 + \frac{\hbar^2\pi^2}{2m_c^*L_z^2} m^2 \quad (1.9)$$

Where m_c^* is the effective mass of electrons in the conduction band.

Initially, electron energy state in conduction band is continuum, when induced the 3-D quantum confinement, the conduction band splits into discrete energy levels, just like the energy distribution in an artificial atom.

Density of state (DOS)

Density of state is the number of states per energy per unit volume in real space.

$$\rho(E) = \frac{dN}{dE} = \frac{dN}{dk} \frac{dk}{dE} \quad (1.10)$$

For a quantum well [6],

$$N^{QW} = 2\pi k^2 \frac{1}{(2\pi/L)^2} \frac{1}{L^2} \quad (1.11)$$

$$\frac{dN^{QW}}{dk} = \frac{k}{\pi} \quad (1.12)$$

$$\frac{dk}{dE} = \frac{m^*}{k\hbar^2} \quad (1.13)$$

$$\rho^{QW}(E) = \frac{dN}{dE} = \frac{dN}{dk} \frac{dk}{dE} = \frac{k}{\pi} \frac{m^*}{k\hbar^2} = \frac{m^*}{\pi\hbar^2} \quad (1.14)$$

When there are more than one confined states in the quantum well, the total density of states are:

$$\rho^{QW}(E) = \sum_{i=1}^n \frac{m^*}{\pi\hbar^2} \delta(E - E_i) \quad (1.15)$$

Where ϑ is the unit step function. Figure 1.8 gives an example of the density of states for bulk, Quantum Well and Quantum Dot.

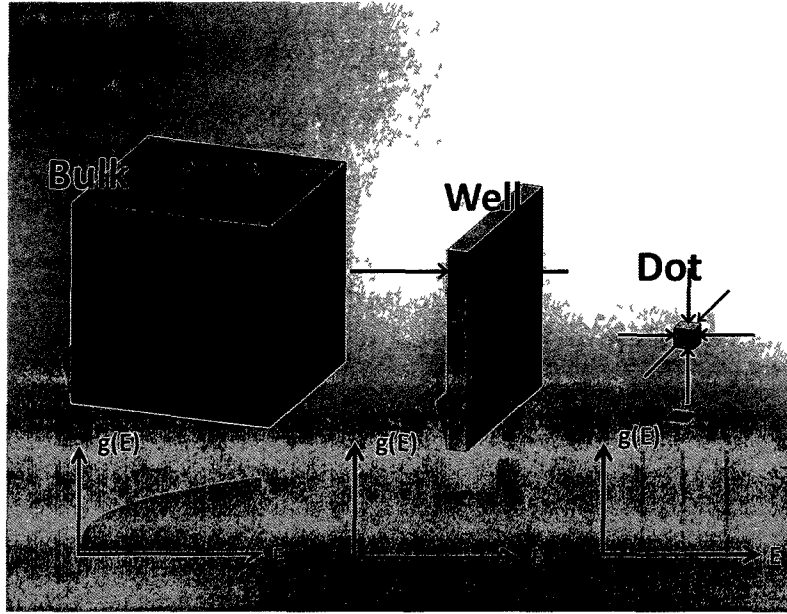


Figure 1. 8 Density of State for Bulk, Quantum Well and Quantum Dot.

For the case of a QD, situation is quite different. Due to the zero-degree freedom, electrons were completely confined within the box, which means there is no dispersion curve. Under this circumstance, the density of state only depends on the number of discrete energy levels. Consequently, the DOS of a QD evolves into the form like a delta-function.

$$\rho^{QD}(E) = g(E_n)\delta(E - E_n) \quad (1.16)$$

Where $g(E_n)$ is the degeneracy of the energy level E_n .

1.1.2.2 Advantages of QDIPs

Sensitive to normal-incident infrared radiation

One of the advantages that QDIP outperforms QWIP is the capability of normal incident sensing. According to Fermi's Golden Rule, the rate of transition can be described as the probability from an initial state to a set of final states [7].

$$P_{in} = \sum_n P(i \rightarrow n) = g(E_1)P(i \rightarrow 1) + g(E_2)P(i \rightarrow 2) + \dots \quad (1.17)$$

Where $P(i \rightarrow n)$ is the probability of transition from initial state to one final state. Due to the transition selection rule, under the normal incident light, transition rate is zero for QWIP, since there is no confined state. Figure 1.9 shows the schematic view of a light incident on the surface of a quantum well with different angles, we can tell that the normal incident light is unable to provide the confinement in the direction where the E-Field oscillate.

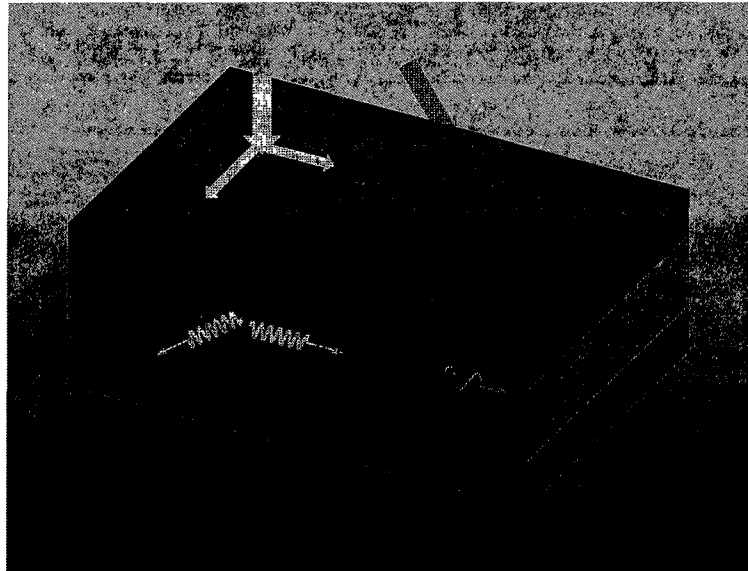


Figure 1. 9 Schematic view (3D) of light incident on a quantum well with different angle

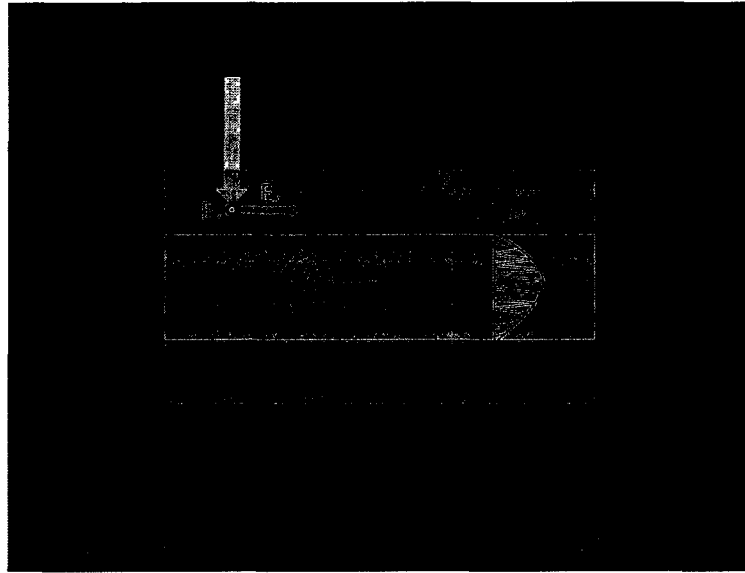


Figure 1. 10 Schematic view of light incident on a quantum well with different angle

Let's take the two energy level electron system as a simple example. E_1 and E_2 , correspond to the wave function $|\varphi_1\rangle$ and $|\varphi_2\rangle$ respectively. The incident light is perpendicular to the plane, and has an electric field E_x along x-axis. It is an “electric dipole” interaction between the photon and the electron [7]. In this case, the electron’s energy will change when it has a displacement x , and the electric dipole momentum is $\hat{\mu} = -ex$, thus, the perturbing Hamiltonian will be [7]:

$$\hat{H}_p = eE_x = -E_x\hat{\mu} \quad (1.18)$$

Where:

$$\mu_{mn} = -e\langle\varphi_m|x|\varphi_n\rangle \quad (1.19)$$

Using the quantized electromagnetic fields, Fermi’s Golden Rule can be restated as [7]:

$$P_{mn} = \frac{2\pi}{\hbar} |\langle\varphi_m| - exE_x |\varphi_n\rangle|^2 \delta(E_f - E_i) \quad (1.20)$$

Because:

$$\hat{\mu} = \begin{bmatrix} \mu_{11} & \mu_{12} \\ \mu_{21} & \mu_{22} \end{bmatrix} \quad (1.21)$$

If $\mu_{mn} = 0$, the probability will be equal to zero, which means it is impossible for the transition.

A quantum box processes the wave function: $|\varphi_m\rangle = \sin\left(\frac{m\pi}{L_x}x\right)$ in x-axis, therefore,

$$\mu_{mn} = -e \left\langle \sin\left(\frac{m\pi}{L_x}x\right) \middle| x \middle| \sin\left(\frac{n\pi}{L_x}x\right) \right\rangle \quad (1.22)$$

Due to the quantization in x direction, the normal incident light can be absorbed and detected by QDIP. Figure 1.11 shows the Lateral-confinement provided by the quantum dot.

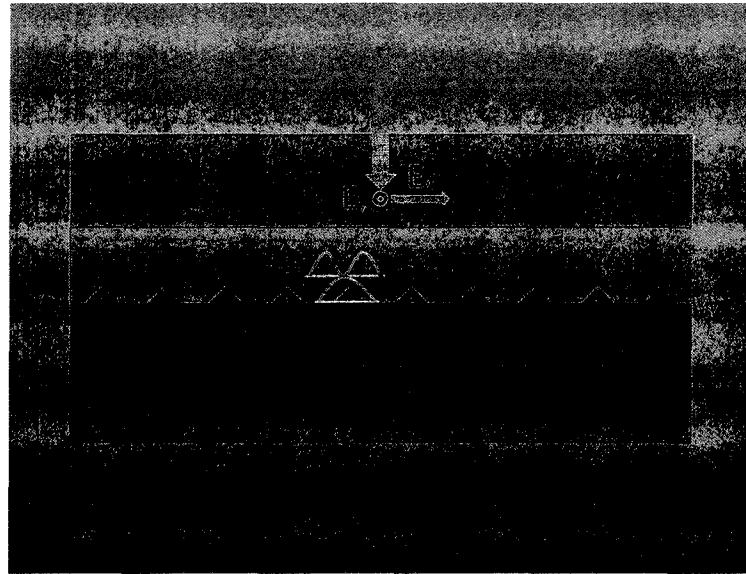


Figure 1.11 Lateral confinement in a pyramid-like quantum dot

Lower dark current

The other attribute of QDIP is the lower dark current. Electrons can be excited not only by an incident photon, but also by the thermal excitation process. Thermal-electrons are the major source of noise current in the detector.

At a stationary state (under zero bias), the thermal generation rate should be equal with the recombination rate, because without the applied electric field, the excited electrons cannot be swept out to form a current, but go back to the bond state after a period τ .

$$R_{th} = R_{re} = \frac{N}{\tau} \quad (1.23)$$

Where N is the number of excited electrons and τ is the life time at the excited state.

When applying a high bias on the detector, the thermal-electrons can be sufficiently collected to the electrode before they relax to the ground state. In this case, all the thermal excited electrons can contribute to the current, which means:

$$qR_{th} = qR_{collect} = I = q \frac{N}{\tau} \quad (1.24)$$

Eq. 1.24 shows the dark current is proportional to the ratio of excited electrons population over the carrier life time.

For a QW, the number of excited electrons is defined as [7]:

$$N_{QW} = \int_{Em}^{\infty} \rho^{QW}(E) F(E) d(E) = \sum_m \int_{Em}^{\infty} \frac{m^*}{\pi \hbar^2} \vartheta(E - E_i) F(E) d(E) \quad (1.25)$$

For a QD,

$$N_{QD} = \rho^{QD}(E)F(E) = \sum_m g(E_n)\delta(E - E_n)F(E) \quad (1.26)$$

As we demonstrated before, the DOS of QD are much less than QW, so the amount of thermal excited electrons in a QD is largely reduced, which results in a lower dark current.

High responsivity

For a photodetector system, the concept of responsivity has been developed as the ratio of electrical output over optical input [7]. (Figure 1.2) shows the geometry of a photoconductor.

Current density:

$$j_{ph} = \Delta n q \mu_n E = \frac{\eta \tau \phi_0}{d} q \mu_n E \quad (1.27)$$

photocurrent:

$$I_{ph} = j_{ph} w d = \eta q \mu_n \tau \frac{w}{l} \phi_0 V \quad (1.28)$$

Responsivity:

$$R = \frac{I_{ph}}{P_{inc}} = \eta \frac{\mu_n \tau}{l^2} \frac{V}{h\nu/q} \quad (1.29)$$

Where τ is the excited carrier life time. Due to the electron-LO phonon scattering process, carriers will relax to the ground state, subsequently, reduced the lift time. However, different from QW, QD has a complete discrete energy levels, which makes the electrons rarely achieved the interaction with LO phonon, thus effectively increases the life time. This phenomenon can be described by the following equation:

$$S_{eg} = \frac{2\pi}{\hbar} |\langle \varphi_e | -eV_{phonon} | \varphi_g \rangle|^2 \rho(E) \quad (1.30)$$

Where V_{phonon} is phonon-induced electrostatic potential, φ_e is the excited state, φ_g is the ground state, and $\rho(E)$ is the density of states. As discussed before, the density of states $\rho^{QD} \ll \rho^{QW}$ (see Figure 1.8), thus the transition rate caused by the LO phonon are largely reduced in QD, consequently, the carrier life time remains longer.

Based on the conclusion above, since the Responsivity is proportional to τ , we can claim that QDIP processes a higher Responsivity than QWIP.

1.2 Plasmonic Enhanced Transmission

Guided by the previous work of Heinz Raether [8], surface plasmon polariton (SPP) has been widely investigated by researchers for decades. It is of interest to scientists in different areas, ranging from physicists, chemists, biologists. Renewed highlight of surface plasmon polariton comes from the recent boost in nano-technology, which gives us the permission to manipulate the metal structure in micro or even nano scale.

For researchers in the area of nanophotonics and optoelectronics, the surface plasmon polariton forms a major part of the fascinating field. One of its most attractive aspects is the so called plasmonic enhanced extraordinary optical transmission (EOT) [9].

1.2.1 What is a Surface Plasmon Polariton

In order to understand what is a SPP, we need to separate the phrase “surface plasmon polariton” into three steps: plasmon, surface plasmon, and surface plasmon polariton.

First of all, the Plasmon. We know that a photon is the quantization of light, a phonon is quantization of mechanical vibration. Following the same rule, a plasmon is a quasiparticle resulting from the quantization of plasma oscillation. To visualize the picture of plasma oscillation, let us imagine a metal jar which is filled by free electrons, applying a constant external electric field directing from right side of the jar to the left. Obviously, under the electric field, the electrons will move to the right side and get together against the sidewall, until they form an inner opposite electric field which neutralizes the external one. If we cut off the electric field, electrons will run back to left

under the influence of Coulomb's Law. Before the energy is exhausted by the collision, this packet of electrons will keep bouncing back and forth between the two sidewalls. The behavior of the electrons packet is called plasma oscillation, the quantization of this oscillation is named as plasmon. Surface plasmon, named after plasmon, can be defined as coherent electron density oscillation but just exist at the interface between two materials.

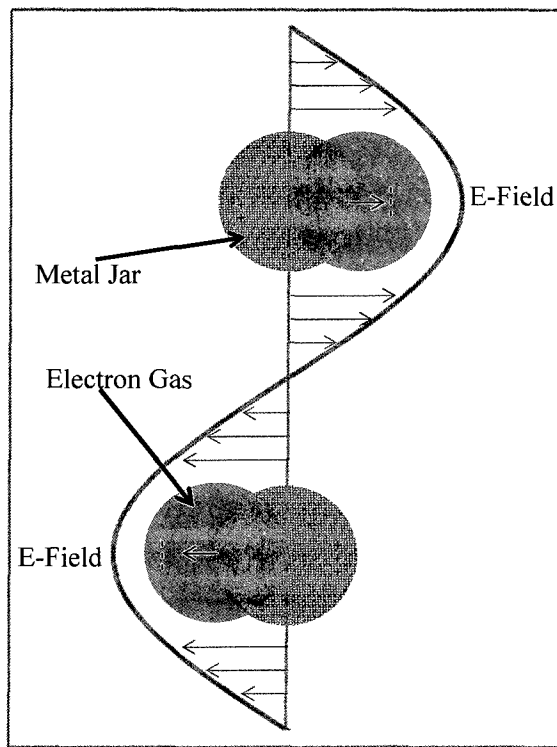


Figure 1. 12 Electron gas movement under the E-Field

Secondly, the Polariton. Polariton is coupling between electromagnetic wave and the electric or magnetic dipole. Thus, the surface plasmon polariton can be understood as the electromagnetic waves coupled to the collective charge oscillation that confined at the boundary [9]. If we go back to the example of free electron jar, this time, we replace the constant field with a sinusoid one. For certain frequencies, the electric field changes too

fast or too slow, consequently, exerts a destructive effect on the movement of the electrons packet. In contrast, if the electric field swings at a particular frequency, which matches the rythme of the electron packet's movement, the energy of the electromagnetic field can be passed from the radiation source to the plasmon; as a special case, the electromagnetic field can be optical radiation. Under this circumstance, the surface plasmon traps the energy of the optical field and creates a self-sustaining, propagating electromagnetic wave, known as the surface plasmon polariton.

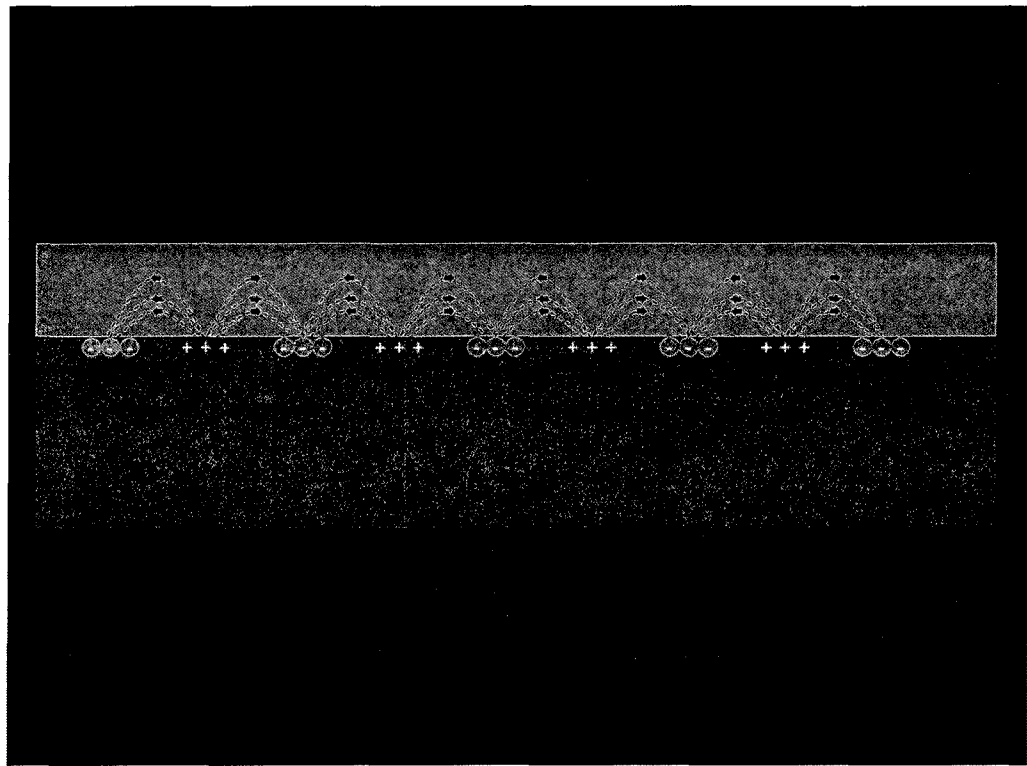


Figure 1. 13 The E-field oscillation at the interface between a metal and a dielectric

1.2.2 Derivation of SPP

From the characteristic description of the surface plasmon polariton, we have established a model that connects the SPPs with a self-sustaining wave propagating at the

interface between a conductor and a dielectric, evanescently confined in the perpendicular direction.

To investigate the properties of SPPs, we have to take the Maxwell's equations as a starting point to establish a physical model for the evanescent wave [10].

$$\nabla \cdot D = \rho_{ext} \quad (1.31a)$$

$$\nabla \cdot B = 0 \quad (1.31b)$$

$$\nabla \times E = -\frac{\partial B}{\partial t} \quad (1.31c)$$

$$\nabla \times H = J_{ext} + \frac{\partial D}{\partial t} \quad (1.31d)$$

In this chapter, we mainly focus on the travelling wave solution in the absence of external stimuli. Thus, the above four equations can be reduced to the following form [10]:

$$\nabla \cdot D = 0 \quad (1.32a)$$

$$\nabla \cdot B = 0 \quad (1.32b)$$

$$\nabla \times E = -\frac{\partial B}{\partial t} \quad (1.32c)$$

$$\nabla \times H = \frac{\partial D}{\partial t} \quad (1.32d)$$

Take the curl of equation (1.32c), it yields

$$\nabla \times \nabla \times E = -\mu_0 \frac{\partial^2 D}{\partial t^2} \quad (1.33)$$

Apply the identity $\nabla \times \nabla \times E = \nabla(\nabla \cdot E) - \nabla^2 E$, equation (1.33) can be transformed into:

$$\nabla(\nabla \cdot E) - \nabla^2 E = -\mu_0 \epsilon_0 \epsilon \frac{\partial^2 E}{\partial t^2} \quad (1.34)$$

Since the divergence of dielectric displacement equals zero ($\nabla \cdot \epsilon E = 0$),

$$\nabla^2 E - \mu_0 \epsilon_0 \epsilon \frac{\partial^2 E}{\partial t^2} = 0 \quad (1.35)$$

In order to make the derivation suitable for the description of confined propagation waves, first, we assume that the electric field is in a harmonic time dependence form $E(r, t) = E(r)e^{-i\omega t}$ [2-3], substituting the E-field into equation (1.35), we obtain the wave equation:

$$\nabla^2 E + k_0^2 \epsilon E = 0 \quad (1.36)$$

Where $k_0 = \frac{\omega}{c}$ is the wave vector of the propagation wave in vacuum.

For simplicity, let us define that the EM wave only propagates along x-direction of a Cartesian coordinate system, meanwhile, it remains constant in y-direction. In this circumstance, the x-y plane coincides to be the interface between a conductor and a dielectric. Thus, the dielectric function ϵ will vary along z direction, which can be described as: $\epsilon = \epsilon(z)$.

Go back to the Maxwell equations, if we apply the harmonic time dependence $(\frac{\partial}{\partial t} = -i\omega)$ to (1.32c) and (1.32d),

$$\nabla \times E = \begin{vmatrix} i & j & k \\ \frac{\partial}{\partial x} & \frac{\partial}{\partial y} & \frac{\partial}{\partial z} \\ E_x & E_y & E_z \end{vmatrix} = \vec{e}_x \left(\frac{\partial E_z}{\partial y} - \frac{\partial E_y}{\partial z} \right) - \vec{e}_y \left(\frac{\partial E_z}{\partial x} - \frac{\partial E_x}{\partial z} \right) + \vec{e}_z \left(\frac{\partial E_y}{\partial x} - \frac{\partial E_x}{\partial y} \right) = i\omega\mu_0 H$$

(1.37a)

$$\nabla \times H = \begin{vmatrix} i & j & k \\ \frac{\partial}{\partial x} & \frac{\partial}{\partial y} & \frac{\partial}{\partial z} \\ H_x & H_y & H_z \end{vmatrix} = \vec{e}_x \left(\frac{\partial H_z}{\partial y} - \frac{\partial H_y}{\partial z} \right) - \vec{e}_y \left(\frac{\partial H_z}{\partial x} - \frac{\partial H_x}{\partial z} \right) + \vec{e}_z \left(\frac{\partial H_y}{\partial x} - \frac{\partial H_x}{\partial y} \right) = -i\omega\epsilon_0\epsilon E$$

(1.37b)

six components of the EM field will be achieved as below [10]:

$$\frac{\partial E_z}{\partial y} - \frac{\partial E_y}{\partial z} = i\omega\mu_0 H_x$$

(1.38a)

$$\frac{\partial E_z}{\partial x} - \frac{\partial E_x}{\partial z} = i\omega\mu_0 H_y$$

(1.38b)

$$\frac{\partial E_y}{\partial x} - \frac{\partial E_x}{\partial y} = i\omega\mu_0 H_z$$

(1.38c)

$$\frac{\partial H_z}{\partial y} - \frac{\partial H_y}{\partial z} = -i\omega\mu_0 E_x$$

(1.38d)

$$\frac{\partial H_z}{\partial x} - \frac{\partial H_x}{\partial z} = -i\omega\mu_0 E_y$$

(1.38e)

$$\frac{\partial H_y}{\partial x} - \frac{\partial H_x}{\partial y} = -i\omega\mu_0 E_z$$

(1.38f)

To keep the consistency with our predefined condition, the field won't change with the y component ($\frac{\partial}{\partial y} = 0$), the above equation series can be updated as [10]:

$$\frac{\partial E_y}{\partial z} = -i\omega\mu_0 H_x$$

(1.39a)

$$\frac{\partial E_z}{\partial x} - \frac{\partial E_x}{\partial z} = i\omega\mu_0 H_y \quad (1.39b)$$

$$\frac{\partial E_y}{\partial x} = i\omega\mu_0 H_z \quad (1.39c)$$

$$\frac{\partial H_y}{\partial z} = -i\omega\mu_0\varepsilon_0\varepsilon E_x \quad (1.39d)$$

$$\frac{\partial H_z}{\partial x} - \frac{\partial H_x}{\partial z} = -i\omega\mu_0\varepsilon_0\varepsilon E_y \quad (1.39e)$$

$$\frac{\partial H_x}{\partial y} = -i\omega\mu_0\varepsilon_0\varepsilon E_z \quad (1.39f)$$

Based on the polarization direction, equation (1.39) can be classified as two set of wave, the TE wave (1.39a, 1.39c, 1.39e) and the TM wave (1.39b, 1.39d, 1.39f).

Let us first consider the TM wave [8]:

for $z > 0$,

$$H_2 = (0, H_{y2}, 0) \exp(i(k_{x2}x + k_{z2}z - \omega t)) \quad (1.40a)$$

$$E_2 = (E_{x2}, 0, E_{z2}) \exp(i(k_{x2}x + k_{z2}z - \omega t)) \quad (1.40b)$$

for $z < 0$,

$$H_1 = (0, H_{y1}, 0) \exp \cdot i(k_{x1}x - k_{z1}z - \omega t) \quad (1.40c)$$

$$E_1 = (E_{x1}, 0, E_{z1}) \exp \cdot i(k_{x1}x + k_{z1}z - \omega t) \quad (1.40d)$$

Take into account the continuity relations [8], when $z = 0$:

$$E_{x1} = E_{x2} \quad (1.41a)$$

$$H_{y1} = H_{y2} \quad (1.41b)$$

$$\varepsilon_1 E_{z1} = \varepsilon_2 E_{z2} \quad (1.41c)$$

From (1.41a), (1.41b), we can achieve the continuity:

$$k_{x1} = k_{x2} = k_x \quad (1.42a)$$

Substitute H_1 and H_2 into (1.39d):

$$ik_{z1}H_{y1} = +i\omega\mu_0\varepsilon_0\varepsilon_1E_{x1} \quad (1.42b)$$

$$ik_{z2}H_{y2} = -i\omega\mu_0\varepsilon_0\varepsilon_2E_{x2} \quad (1.42c)$$

Insert (1.41b) into (1.42):

$$E_{x1} = \frac{ik_{z1}H_{y1}}{i\omega\mu_0\varepsilon_0\varepsilon_1} = E_{x2} = -\frac{ik_{z2}H_{y2}}{i\omega\mu_0\varepsilon_0\varepsilon_2} \quad (1.43)$$

Together with (1.41b), a relationship between k_{z1} k_{z2} ε_1 ε_2 has been claimed as

[8]:

$$\frac{k_{z1}}{\varepsilon_1} + \frac{k_{z2}}{\varepsilon_2} = 0 \quad (1.44)$$

Transform equation (1.35) to harmonic time dependence form and expend the divergence operator into its differential state:

$$\left(\frac{\partial^2}{\partial x^2} + \frac{\partial^2}{\partial y^2} + \frac{\partial^2}{\partial z^2} \right) E + k_0^2 \varepsilon \cdot E = 0 \quad (1.45)$$

Since $E_i = E_{0i} \cdot \exp \cdot i(k_x x + k_z z - \omega t)$, and the EM field remains constant in y-direction ($\frac{\partial}{\partial y} = 0$),

$$(ik_x)^2 + (ik_{zi})^2 + \varepsilon \left(\frac{\omega}{c}\right)^2 = 0 \quad (1.46)$$

Combine equation (1.44) together with (1.46),

$$k_x = \frac{\omega}{c} \sqrt{\frac{\varepsilon_1 \varepsilon_2}{\varepsilon_1 + \varepsilon_2}} \quad (1.47)$$

From (1.47), we identified the condition to support surface Plasmon polariton propagate on the interface between two materials. [8]

1.2.3 Excitation of Surface Plasmon Polaritons

When talking about the properties of SPPs, we need to start from the dispersion curves of it.

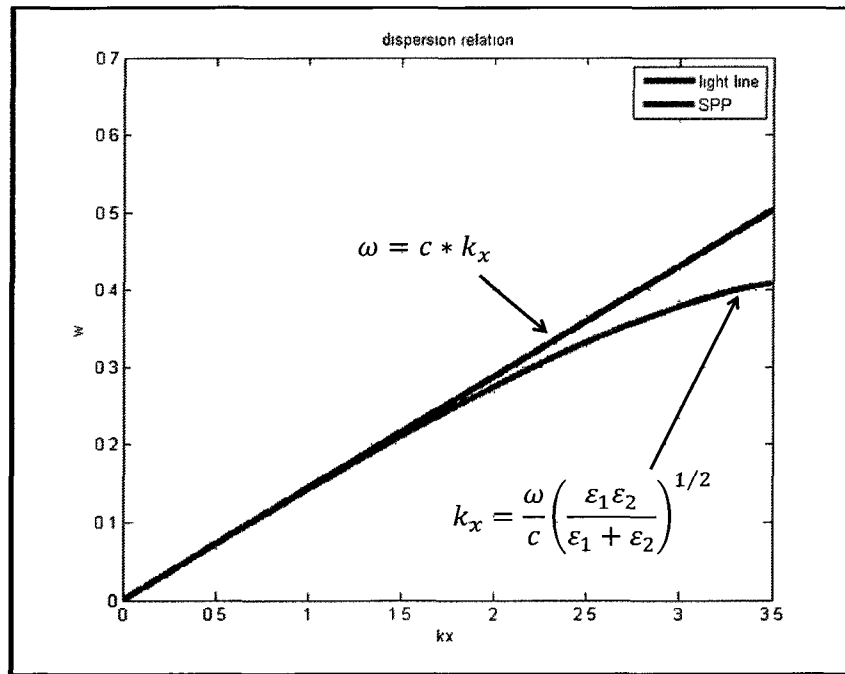


Figure 1. 14 Dispersion relation of SPPs at the interface between metal and air

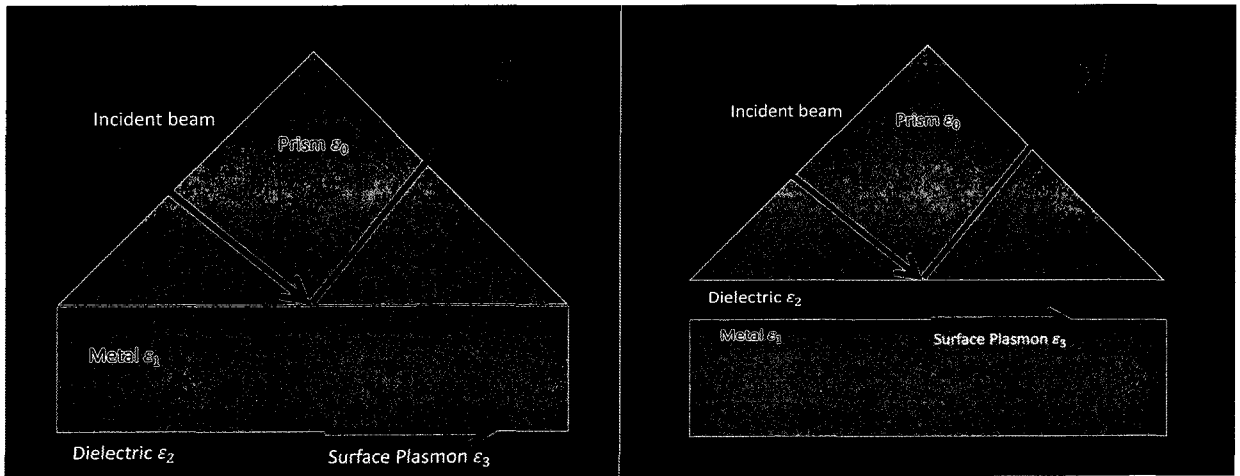
In the figure above, we can clearly see the dispersion relationship between bulk plasmon polariton, surface plasmon polariton and photon. The surface plasmon on the

interface between metal and air cannot be excited, since it lies to the right side of the photon line [10].

The most commonly used techniques for SPP excitation can be classified as two categories, one is impacting charged particles, and the other is using optical phase-matching method. In this paper, we focus on the optical phase-matching technique, especially the coupling by gratings.

1.2.3.1 Prism Coupling

As mentioned before, at the interface between metal and air, SPPs is unable to be excited due to the wavevector mismatching issue, for the incident photons under an angle θ to the surface normal, the momentum projection along the interface $k_{x-ph} = k \sin \theta$ is always smaller than the SPPs' propagating constant k_{x-SPPs} [8]. This phenomenon can be easily identified from Figure 1.15, under the same frequency ω , the SPP dispersion curve is on the right side of the photon. To realize the excitation, we need to find a way that can helps the photon to increase its wavevector along the plane [8].



a)

b)

Figure 1. 15 Prism coupling to SPPs through attenuated total internal reflection in the Kretschmann (a) and Otto (b) configuration.

The essential idea of the prism-coupling method is to achieve a compensation of the photon's momentum that parallel to the x-direction [9]. When shining a light into the prism under a certain angle, the total internal reflection occurs at the boundary between the glass and metal, thus an evanescent wave emerges with a phase velocity $v = \omega/k_x = c/(\sqrt{\epsilon_0} \sin \theta_0)$. The photon line $\omega = ck_x/(\sqrt{\epsilon_0} \sin \theta_0)$ in this case has been tilted by a factor of $\sqrt{\epsilon_0} \sin \theta_0 > 1$ compared with the frequency $\omega = ck_x$. As a consequence, the resonant condition can be fulfilled.

1.2.3.2 Grating Coupling

Another way to overcome the mismatch of the wave vector between the in-plane momentum of SPP and of the incident photon is utilizing the diffraction effect. Normally, a bragg grating can be applied to realize the compensation. First of all, let us have a quick review of the light diffracted by a grating as demonstrated in Figure 1.16.

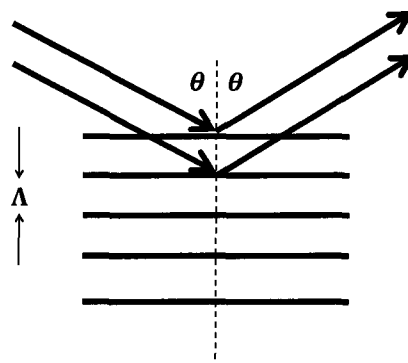


Figure 1. 16 Light diffracted by a grating

The incident light from the grating would generate a bragg peak if their reflections from different interface interfered constructively, which indicates that all the phase shift should be an integer times of 2π .

$$2n\Lambda \sin\theta = m\lambda \quad (1.48)$$

Where n is the refractive index between two interfaces, Λ is the lattice constant of the grating, m is an integer. Meanwhile, the wave vectors of the incident light, reflected light and the grating vector should remain conserved.

$$\vec{k}_{re} = \vec{k}_{in} + \vec{G} \quad (1.49)$$

Where $\vec{G} = \frac{2\pi}{\Lambda}$ is the grating vector. Figure 1.17 also demonstrates the conservation relationship of the three vectors.

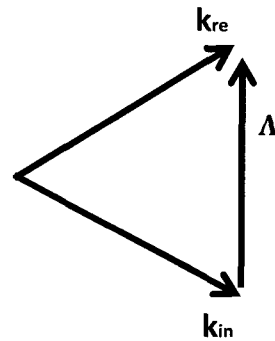


Figure 1. 17 Wave vector conservation

Based on the discussion above, it is possible to generate a SPP mode by impinging light on the gratings, since the sum of grating vector and the in-plane vector of incident light will matches the excitation condition once it reaches a specific value.

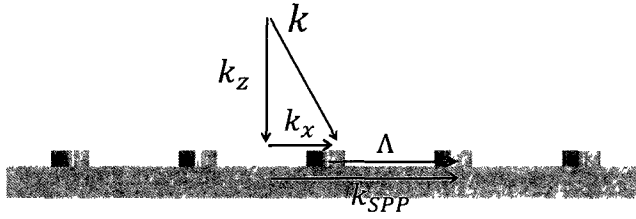


Figure 1. 18 the excitation of SPP by gratings

$$|\vec{k}_{SP}| = \left(\frac{\omega}{c}\right) \sqrt{\frac{\epsilon_1 \epsilon_2}{\epsilon_1 + \epsilon_2}} = |\vec{k}_x \pm n \vec{G}_x| \quad (1.50)$$

Equation (1.50) illustrates the most simplest condition for launching a SPP mode on an air-metal interface.

1.2.4 Extraordinary Optical Transmission 2DMHA

The extraordinary optical transmission (EOT) was first been reported by Ebbesen in 1998 [11]. For a metal screen perforated with a single subwavelength aperture, the transmission is relatively low and has been proved to be proportional with the fourth power of the ratio of diameter over wavelength $\left(\frac{d}{\lambda}\right)^4$ [22]. While, if we spread the hole in both x and y direction and structure them into a periodic array with a constant lattice, the transmission will experience a significant increasing as demonstrated in Ebbesen and his co-worker's work. At certain wavelengths, $T(\lambda)$ can be larger than 1, after normalized the transmission of the total hole arrays to a unit open area, enhancement ratio would be up to three orders of magnitude compared with the transmission through the single aperture

[12]. The mechanism which leads to the enhancement could be attributed to the SPPs excited by the grating (2D hole array).

However, even if it is asserted that the SPP has played a crucial role in the enhanced transmission process, a detailed interpretation is still under debated. Several kinds of theories have been applied to make it clear and reasonable [12], such as the resonant transfer of SPP mode from one interface to another, penetration of the SPP from one interface to the other through the holes, localized field inside the holes, and the SPP Bloch Waves tunneling through a film.

1.2.4.1 Resonant Light Tunneling

One of the popular explanations on this phenomenon is the resonant light tunneling effect. Analogous to the well-known theory, the resonant tunneling through a barrier by an electron, a photon is also capable to be transferred from one side of the metal film to the other, consequently contributes to the transmission intensity. The media that supports the photon to travel through the “barrier” is the SPP mode. In the microscopic view, the incident photon first hits on the gratings, build-up its in-plane wavevector k_x to a specific value, when this value matches with the condition for the SPP to be excited on the interface, the energy of the photon will couple to the SPP state, after that, the surface mode on the input side will evanescently couple to the output side, and then scatter back to the light state after tunnel through the film. It should be noticed that the coupling can exists in three different conditions, the first one is coupled to the SPP mode on the air-metal surface; second, instead of couples to the top surface, the light may also weakly transmitted through the array and coupled to the SPP mode on the opposite side of the film; thirdly, both of the SPP modes on each surface are excited

under certain condition, and the two modes interact with each other. For the latter one, the simultaneous excited modes should be called double resonance SPPs [13], compared with the one side coupling, the transmission enhancement for the latter one could be larger.

1.2.4.2 Localized Surface Plasmons

Recent investigations have claimed that the “shape resonances” of an aperture can also be counted as an important factor for transmission enhancement [13]. Except for the contribution of SPPs, Localized Surface Plasmons (LSP) also help to increase the transmission efficiency [15]. The activation of LSP can be proved by examine the transmission properties of rectangular holes on a metal screen. Via rotating the angle between polarization direction and the edge of the hole (from 0 to 2π), two distinct peaks can be observed. Since the LSP can only oscillate along the direction that perpendicular to the electric field (magnetic dipole), the switching between two peaks indicate that the LSP has been excited by the incident field when its polarization direction is orthogonal to the edge of the rectangular hole [14].

II. GROWTH, FABRICATION AND TEST

2.1 Growth

2.1.1 Growth Technology (MBE)

One of the most commonly used techniques to obtain Quantum Wells and Quantum Dots devices is Molecular Beam Epitaxy (MBE) [5]. Impinging a ‘molecular beam’ which contains a special material on to the substrate, MBE can create the crystal by depositing the atoms layer by layer. The atomic-level growth provide us a more accurate way to control the properties of our devices, in the meantime, slow deposition rate requires high vacuum level in order to keep a pure growth environment.

Self-assembled InAs quantum dots device is also grown by MBE using the Stranski-Krastanov (SK) method. After inducing a lattice mismatch between different materials such as InAs on GaAs, strains was accumulated [19]; when the thickness of the atom film reaches the critical value, the shape will be damaged and the edge dislocation will appeared [5], in that way, a quantum dot is formed due to the inherent behavior of the material to relax stress.

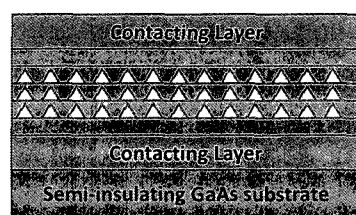
2.1.2 Growth Condition and Process

Our QD samples are grown by using a V80H molecular beam epitaxy (MBE) system. Firstly, a 100 nm undoped GaAs buffer layer was formed right above the substrate, a semi-insulating GaAs (100) wafer; after that, a $0.3\mu\text{m}$ Si-doped (n^+) GaAs contact layer ($n = 1 \times 10^{18}\text{cm}^{-3}$) was deposited on the buffer layer. The active region for our detector is formed by 10 periods of InAs quantum dots absorption layer with spacer layers of GaAs sandwiched in between. Each QD layer included 1 nm $\text{In}_{0.15}\text{Ga}_{0.85}\text{As}$ and

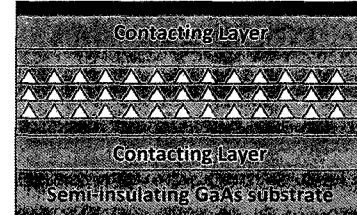
2 monolayers (ML) of InAs QDs, the thickness of GaAs spacer was 50 nm. The top contact layer was Si-doped ($n=1\times10^{18}\text{cm}^{-3}$) GaAs layer with the thickness of 0.1 μm .

2.2 Fabrication

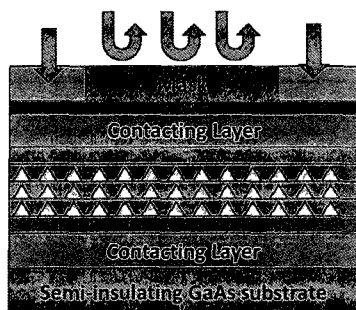
The fabrication process of Infrared Quantum Dot Photodetectors is schematically demonstrated in Figure 2.1a through Figure 2.1j [5]:



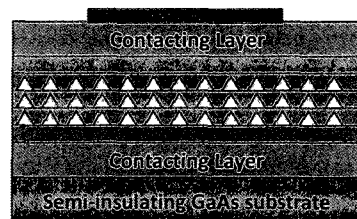
2.1a)



2.1b)



2.1c)



2.1d)

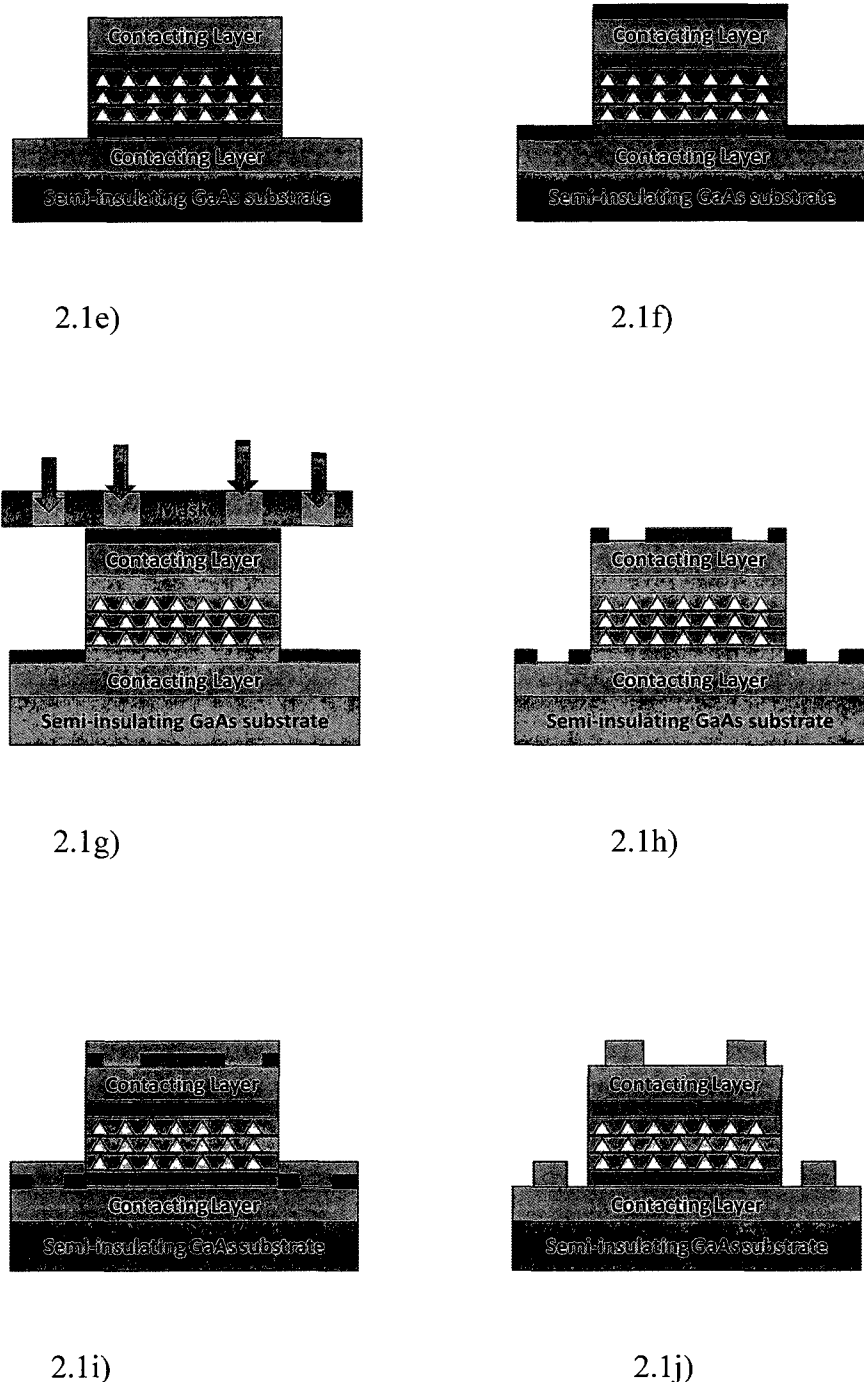


Figure 2.1 QDIP fabrication

When the semiconductor growth (MBE growth) was finished, fabrication of QDIPs was processed in cleanroom. First of all, to get rid of the surface dusts and grease, the wafer should be cleaned in ultrasonic bay; then, a layer of positive photoresist had been spin-coated on the top surface; after that, the sample was placed on a hot plate with constant temperature 100 °C for soft bake; to obtain the desired patterns, the wafer was covered by a photomask and exposed with UV light, the photomask can let the light pass through the open channel and block out the light that hit on the dark area; positive photoresists became soluble after exposed in UV light, once been dipped into the developer (CD-30), the area protected by mask remained the same, but the part under exposure was washed away, therefore, the patterns had been transferred from the mask to the wafer. In the next step, the wafer was then wet-etched in a particular solution, the QDIPs mesas were formed in this process. The wafer was then rinsed by DI water, spin-coated and soft baked again as before. Then we applied the other photomask, align it with the mesa array, and exposed once again, the metal electrode pattern was imprinted on the wafer. Finally, metal alloy was deposited on the sample, lift-off was operated, and Rapid Thermal Annealing was done as the last step.

2.3 Test Setup

2.3.1 Spectral Response Measurement of QDIPs

Typically, the spectrum response of a standard QDIP is obtained by measuring the FTIR spectrometer signal. FTIR stands for Fourier Transform Infrared, Figure 2.2 shows the schematic view of a FTIR spectrometer. Blackbody source, 50% beam splitter, moving mirror, fixed mirror and an Infrared Photodetector are the main components of a typical FTIR spectrometer.

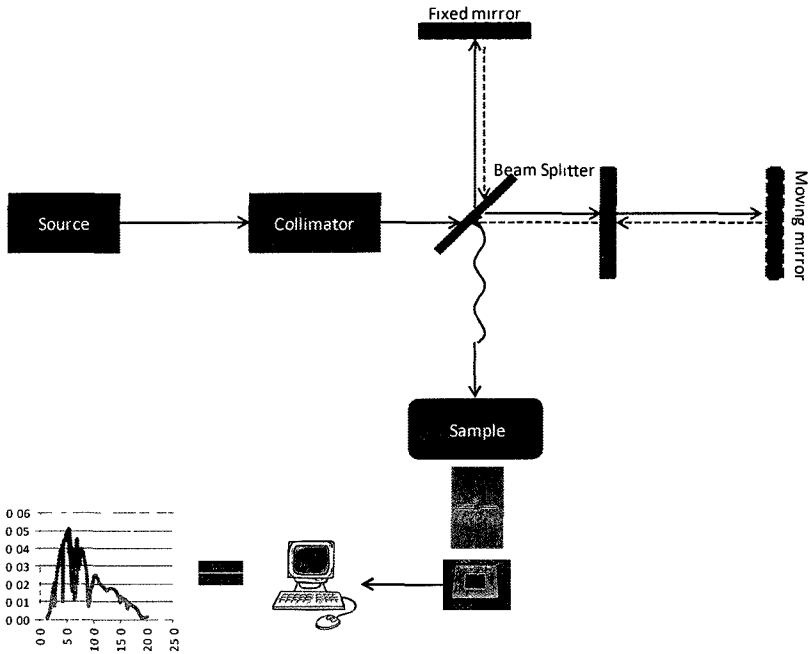


Figure 2.2 the schematic view of FTIR spectrometer

During the operation of each scan, the beam splitter took the incoming IR light and divided it into two paths, heading to the fixed and moving mirror respectively. The two reflected beam recombined when back to the splitter and passed through a sample. Due to the constantly changed optical path difference induced by the moving mirror, the two beams interfered with each other and consequently generated an interferogram. Different from the normal optical or UV spectrometer, each point of the FTIR interferogram contained all the frequency information from the blackbody source. The interference of those two beams can be described as below:

$$I(x) = |E_1 + E_2|^2 = E_1^2 + E_2^2 + 2E_1E_2 \cos(\delta) = \frac{I_0}{2} + \frac{I_0}{2} \cos\left(\frac{2\pi}{\lambda}x\right) \quad (3.1)$$

Where I_0 is the intensity of the incident light, x is the optical path difference induced by the moving mirror and λ is the wavelength. The $I(x)$ can also be expressed as:

$$I(x) = \int_0^{\infty} \frac{I_0}{2} \left[1 + \cos\left(\frac{2\pi}{\lambda} x\right) \right] G(\lambda) d\lambda \quad (3.2)$$

In equation (3.2), $G(\lambda_0)$ is actually the transmission performance of the sample at a specific wavelength λ_0 . If we take the reverse Fourier Transform of the AC part from (3.2), the transmission profile will be obtained:

$$G(\lambda) = \int_{-\infty}^{+\infty} I(x) \exp\left(-j\left(\frac{2\pi}{\lambda} x\right)\right) dx \quad (3.3)$$

By replacing the internal IR detector with the QDIPs, the spectral response of our device can be measured with the assistance of external pre-amplifier. The schematic set up diagram is demonstrated in Figure 2.3. Firstly, the sample was mounted into the cooling chamber (Janis, Model No.: ST-100) and connected to the outside circuit which applied voltage on the sample. Then the chamber was inserted into the FTIR body (Bruker, Tensor27), IR beam had been aligned on the mesa surface afterward. Bias voltage was provided by pre-amplifier (Standford research systems, model SR570), operating temperature was well controlled by the temperature controller (Lakeshore, 331 Temperature Controller) connects to the chamber to adjust temperature.

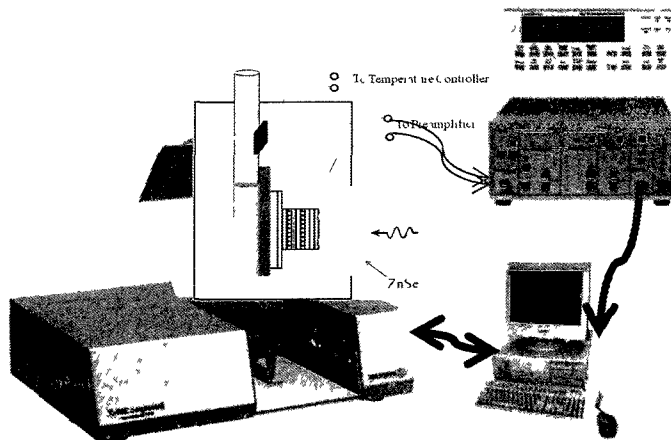


Figure 2. 3 The schematic diagram of spectral response testing setup for QDIPs.

2.3.2 Photocurrent Measurement of QDIPs

Photocurrent is the current in the IR detector that responses to the black body radiation. Once the active material absorbed the photon energy, excess carriers are generated inside the device and the overall conductivity has been increased. As a result, an extra amount of current flows through the device, which is the Photocurrent.

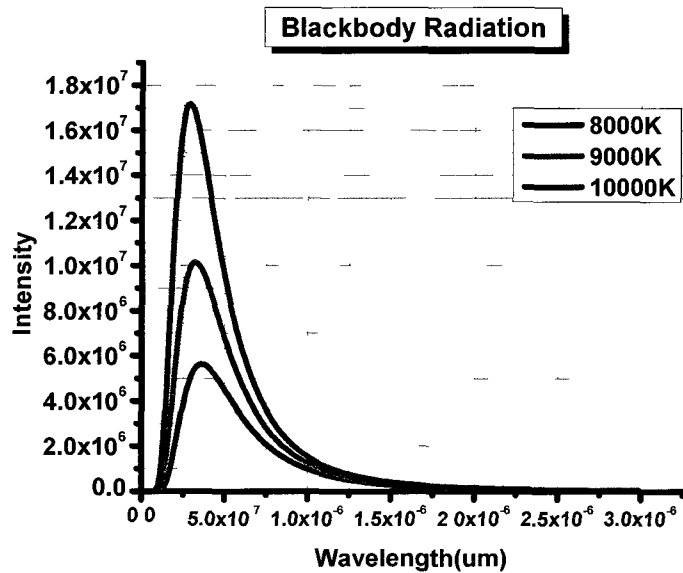


Figure 2. 4 Black body radiations at different temperature.

During the measurement of photocurrent signal, a blackbody radiation was placed in front of the chamber, which worked as the light source and emitted infrared light. An external chopper was mounted between the radiation source and the chamber, modulated the incident light in a desired frequency (usually 590-600Hz). A bandpass optical filter ($2.4\mu\text{m}$, $3.6\mu\text{m}$, $4.5\mu\text{m}$, $7\mu\text{m}$) was also put on the window of the chamber, blocking out the radiation energy from the region that we were not interested in. Finally, the filtered light reached the device through a ZnSe window ($3-14\mu\text{m}$, Transmittance = 60%). The photocurrent generates in the device flows by electrical field that set up by preamplifier.

The photocurrent was collected and amplified by pre-amplifier, then out to the spectrum analyzer (Standford Research Systems, Model SR760). The spectrum analyzer then picked up the photocurrent value at 593Hz to avoid the 1/f noise.

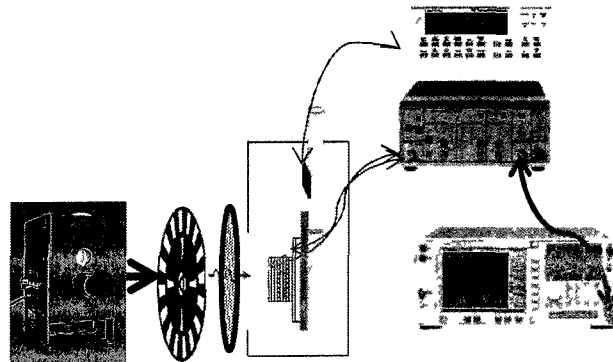


Figure 2. 5 Photocurrent test set up in CMOS lab.

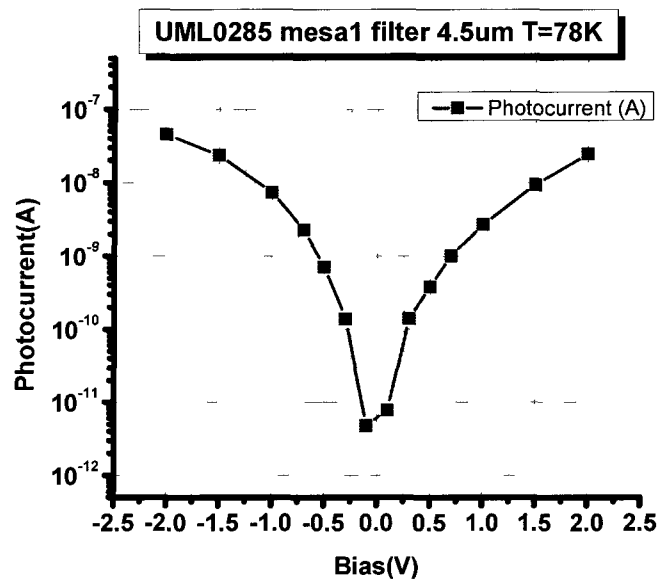


Figure 2. 6 Photocurrent tested on sample UML0285.

Figure 2.6 shows the photocurrent of a sample that been tested by the system. The bandpass filter was $4.5\mu\text{m}$, operating temperature was 77K, blackbody radiation emitted at 1000K, chopper modulated as 593Hz.

2.3.3 Dark Current and Noise Current Measurement of QDIPs

As the main source of noises in an IR detector, dark current has a great impact on the performance of the QDIPs. A common way to measure this parameter is using the source meter. When the test proceeded to the step of dark current, to eliminate the IR radiation from the environment, the chamber was covered with the Aluminum foil and totally isolated from the external optical field. After cooling down to the desired temperature (77K) with liquid nitrogen, voltage and current were kept recorded simultaneously as the bias voltage supplied by our source meter (KEITLEY 2602) increased between two predetermined points. As showed in Figure 2.7, the I-V curve was generated by plotting each data point of the current-voltage pair.

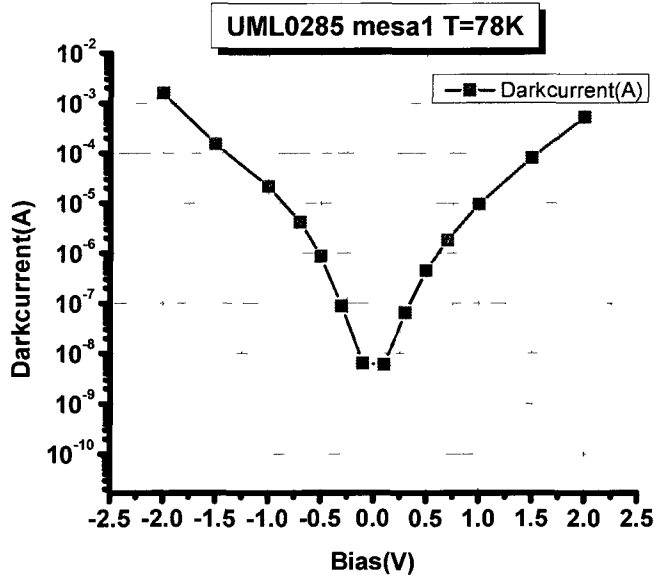


Figure 2. 7 Dark current of QDIPs measured by source meter.

Noise current is defined as the spectral density of dark current, in order to measure this parameter, a fast Fourier transform (FFT) spectrum analyzer had been applied during the test. As described above, the chamber was kept under low temperature

and eliminated from the light outside, current was stimulated and amplified by the pre-amplifier, sent to the spectrum analyzer (Standford Research Systems, Model SR760), finally expended as dark current spectrum. Figure 2.8 is the schematic view of the noise current setup diagram.

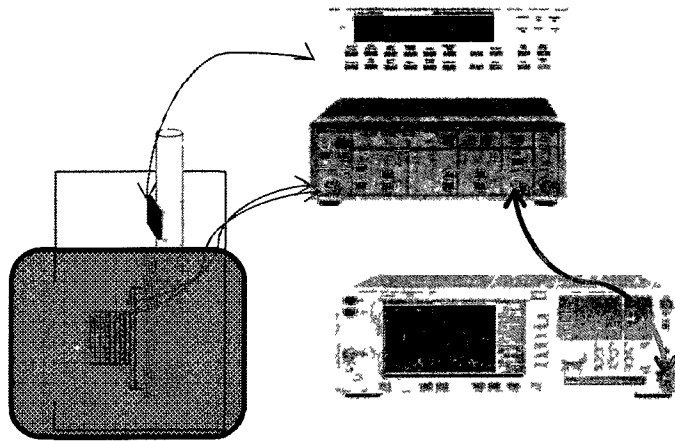


Figure 2. 8 The schematic view of noise current setup.

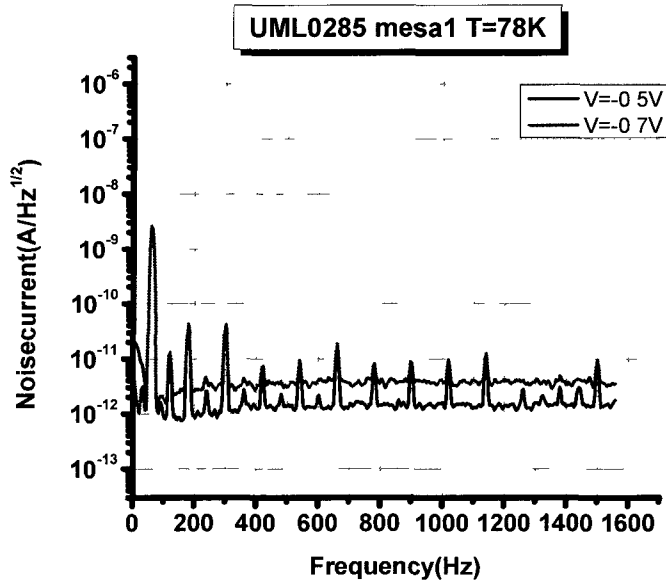


Figure 2. 9 Dark current spectrum under different bias voltage.

Figure 2.9 is the dark current spectrum under different bias voltage. The 1/f noise dominated at low frequency, in order to minimize it, the noise currents (i_{noise}) at high frequency (593Hz) were measured.

III. SPP ENHANCED QDIP

Quantum Dot Infrared Photodetectors (QDIPs) possess several prominent characteristics that make it outperformed the Quantum Well Infrared Photodetectors (QWIPs) [3], such as capability of detection normal incident light; higher photoconductive gain and photoreponsitivities; lower dark current and reduced dependence of the carrier distribution on the temperature. However, QDIPs also have shortcomings, one of the major issue is the limited number of active layers (QDs layer) that can be stacked into the device. Leading by the accumulation of strain in the growth process, crystal defects and dislocations are inevitable, to keep the material working at a good state, we have no choice but to make the absorption layer thin, in another word, only a small fraction of the total energy can be involved in the interaction of the photon detecting. Surface Plasmon Polariton can successfully couple the incident light field, transfer it into the plasmon wave, and keep the optical field been focused near the surface. Such a technology gives us the permission to trap the energy near the dots layer and increase the percentage that been absorbed by electrons. Following the pioneer work by TW Ebbesen [11], researches have been extensively focused on the extraordinary optical transmission (EOT) and its applications. By integrating a metal film perforated with 2 dimensional subwavelength hole arrays on the top of a detector, great improvement of photocurrent can be observed and identified through standard testing procedure.

3.1 Transmission Properties of 2D Metal Hole Arrays on GaAs

3.1.1 Excited by Periodic Hole Arrays

According to Chapter 2, the incident light is unable to be directly coupled to surface plasmons on a smooth metal-dielectric interface, due to the dispersion relationship of SPPs between metal and air. Since the dispersion curve of SPPs lies outside of the light line, from Figure 3.1, the momentum of SPs is greater than the momentum of photon under same frequency. However, a periodic structure makes it possible to let those two momentums match with each other, by adding the grating momentum [16], thus:

$$k_{SP} = k_x \pm nG_x \pm mG_y \quad (3.1)$$

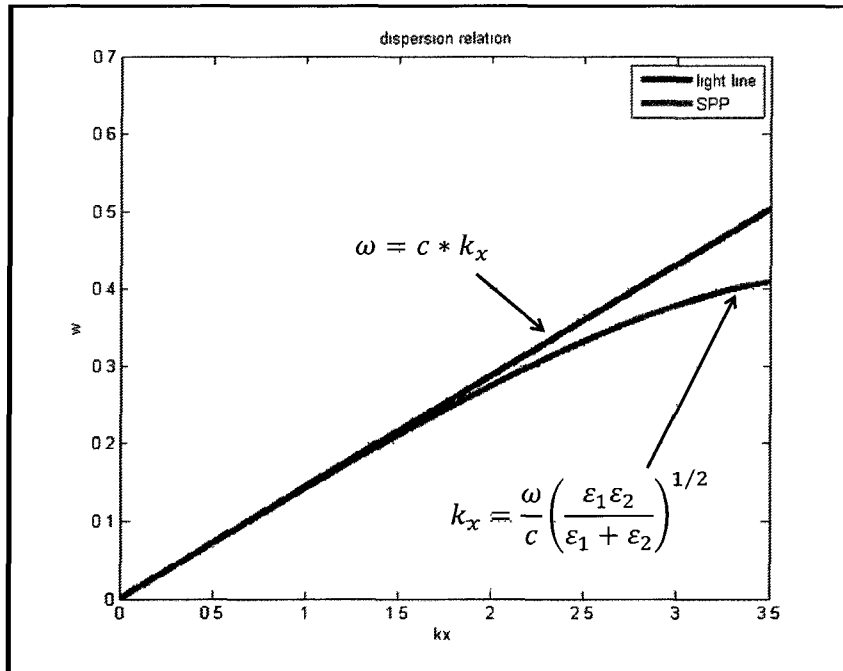


Figure 3. 1 Dispersion relationship of SPP and photon.

Figure 3.2 shows the 2D metal hole array fabricated on GaAs wafer by standard photolithography, the metal is Au, thickness is 30nm.

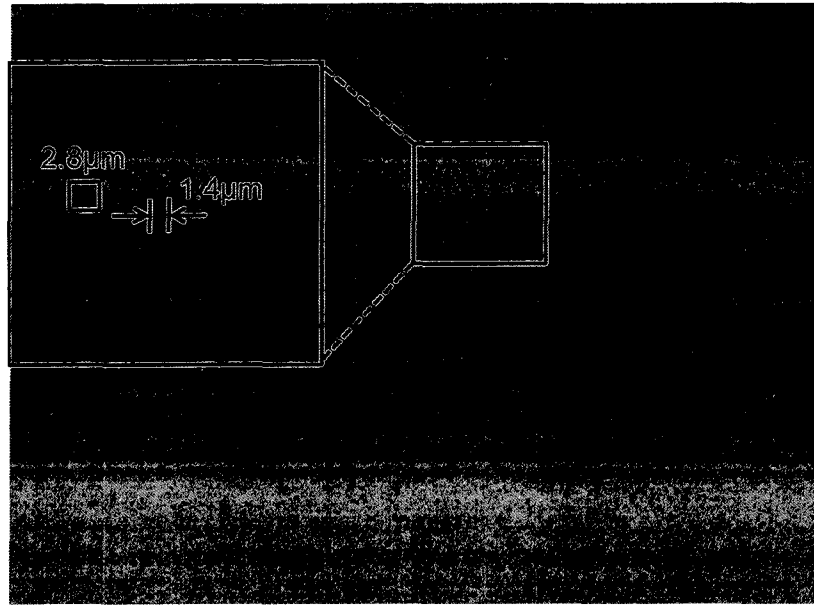


Figure 3. 2 2D hole array perforated on Au film, period 2.8μm, hole size 1.4μm.

3.1.2 Wavelength Selection---Lattice Constant Variation

Based on the derivation in Chapter 1, the condition to support SPs wave propagating on the interface of two media is:

$$k_{SP} = \left(\frac{\omega}{c}\right) \sqrt{\frac{\epsilon_1 \epsilon_2}{\epsilon_1 + \epsilon_2}} \quad (3.2)$$

For simplicity, let us first consider the normal incidence, where $k_x = 0$, consequently:

$$|k_{SP}| = \sqrt{(nG_x)^2 + (mG_y)^2} \quad (3.3)$$

Assume the periods in x and y direction are uniform, thus, $G_x = G_y = \frac{2\pi}{a}$, substitute (3.2) into (3.3), we get:

$$|k_{SP}| = \sqrt{n^2 + m^2} \frac{2\pi}{a} = \left(\frac{2\pi f}{c}\right) \sqrt{\frac{\epsilon_1 \epsilon_2}{\epsilon_1 + \epsilon_2}} \quad (3.4)$$

$$\lambda_{SP} = \frac{a}{\sqrt{n^2+m^2}} Re \left(\sqrt{\frac{\varepsilon_1 \varepsilon_2}{\varepsilon_1 + \varepsilon_2}} \right) \quad (3.5)$$

From equation (3.5), the SPs resonance wavelength is highly depends on the lattice constant a , the orders of grating vectors m and n , the dielectric constant of the two medias ε_1 and ε_2 .

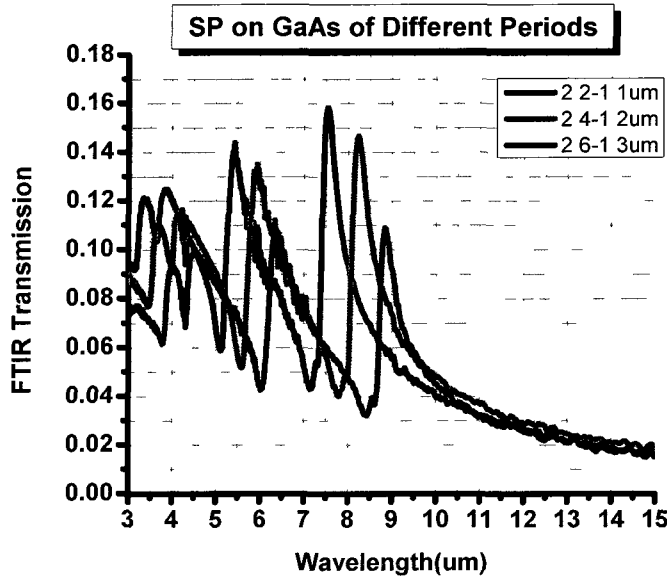


Figure 3.3 Transmission profile of the 2D Metal Hole Array.

Figure 3.3 shows the transmission profiles of 2D metal hole arrays with different lattice constant a . For the Plasmonic mode with same order, for instance (1,0) mode (or its degeneracy (0,1)) and (1,1) mode, the resonance wavelength experienced red shift in the spectrum when the lattice constant increased from 2.2um to 2.6um.

3.1.3 Doping Effect---Dielectric Constant Variation

As demonstrated in Chapter 2, the electron gas inside a bulk material can oscillate under the influence of an incident electromagnetic wave, with the relaxation time τ , thus we can use a simple equation to describe the motion of the plasma sea[10]:

$$m \frac{d^2x}{dt^2} + m \frac{1}{\tau} \frac{dx}{dt} = -eE \quad (3.6)$$

Where $E(t) = E_0 e^{-i\omega t}$ is the driven field, m is the mass of the electron gas.

Assume that $x(t) = x_0 e^{-i\omega t}$, insert into equation (3.6), we obtain:

$$x(t) = \frac{e}{m(\omega^2 + i\frac{1}{\tau}\omega)} E(t) \quad (3.7)$$

The displacement of electron gas leads to a polarization $P = -n e x(t)$, substantially, the dielectric displacement can be demonstrated as

$$D = \epsilon_0 E + P = \epsilon_0 E(t) - \frac{n e^2}{m(\omega^2 + i\frac{1}{\tau}\omega)} E(t) \quad (3.8)$$

Noticing that the plasma frequency of the free electron gas is $\omega_p^2 = \frac{n e^2}{\epsilon_0 m}$, then (3.8)

can be transformed into:

$$D = \epsilon_0 \left(1 - \frac{\omega_p^2}{\omega^2 + i\frac{1}{\tau}\omega} \right) E(t) = \epsilon(\omega) E(t) \quad (3.9)$$

The complex form $\epsilon(\omega) = \epsilon_0 \left(1 - \frac{\omega_p^2}{\omega^2 + i\frac{1}{\tau}\omega} \right)$ can be expressed as $\epsilon(\omega) = \epsilon_r(\omega) + i\epsilon_i(\omega)$, where:

$$\epsilon_r(\omega) = 1 - \frac{\omega_p^2}{\omega^2 + \left(\frac{1}{\tau}\right)^2} \quad (3.10a)$$

$$\epsilon_i(\omega) = \frac{\frac{1}{\tau}\omega_p^2}{\omega^3 + \left(\frac{1}{\tau}\right)^2 \omega} \quad (3.10b)$$

Since the plasma frequency is $\omega_p^2 = \frac{ne^2}{\epsilon_0 m}$, by changing the carrier concentration n [17, 18], we will obtain a different $\epsilon_r(\omega)$, consequently, the Plasmonic resonant wavelength will be tuned.

$$\lambda_{SP} = \frac{a}{\sqrt{n^2+m^2}} \left[\frac{\left(1 - \frac{ne^2}{\epsilon_0 m}\right) \epsilon_2}{1 - \frac{ne^2}{\omega^2 + \left(\frac{1}{\tau}\right)^2 + \epsilon_2}} \right]^{\frac{1}{2}} \quad (3.11)$$

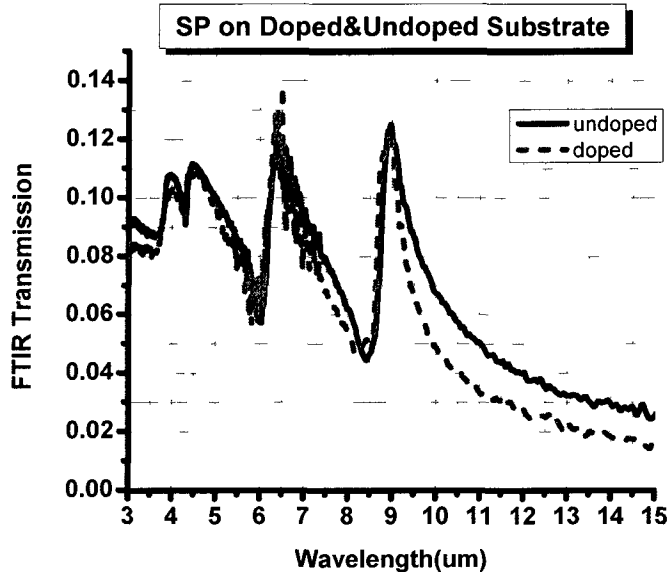


Figure 3. 4 transmission profile of 2D metal hole array on GaAs with different doping level.

Based on the discussion above, we fabricated the 2 D metal hole array on undoped and doped GaAs ($n = 5 \times 10^{18}$) substrate respectively, and measured the transmission profile using FTIR, Figure 3.4 shows a resonant wavelength shift.

3.1.4 Filling Factor Effect---Hole Size Variation

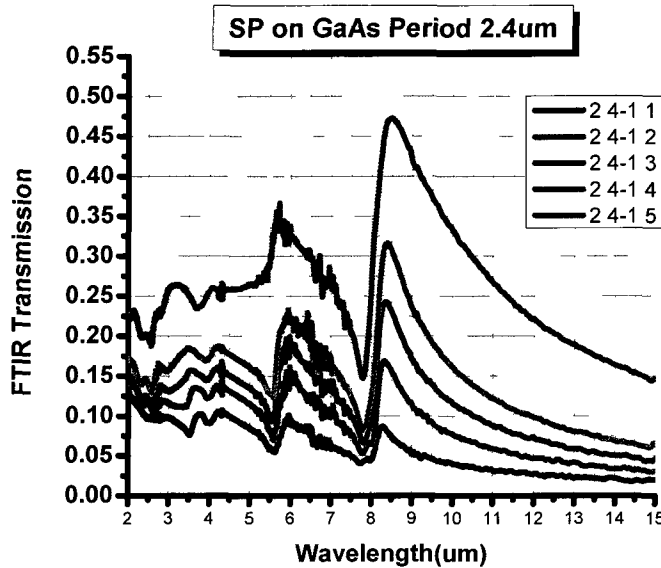


Figure 3. 5 transmission profile of 2D metal hole arrays with different hole size.

Figure 3-5 shows the transmission profile of 2DMHA with the same period ($2.4\mu\text{m}$) but different hole size ($1.1\mu\text{m}$, $1.2\mu\text{m}$, $1.3\mu\text{m}$, $1.4\mu\text{m}$, $1.5\mu\text{m}$). The intensity experienced large increase when the diameter of the hole enlarged from $1.1\mu\text{m}$ to $1.5\mu\text{m}$.

Figure 3-6 demonstrated the relationship between hole diameter versus peak value. This data trendline shows a good linearity and the coefficient of determination R^2 is nearly 0.99, except for the last point (hole diameter equals $1.5\mu\text{m}$), which may result from the fabrication process.

FWHM spectral width stands for the loss of SPPs during the propagation, in Figure 3-7, the linear relationship between hole diameter and FWHM value indicate that along with the enlargement of the dimension of the hole, the loss of SPPs trapped near the surface increases, and more energy has been flowed out.

Quality factor Q is an important parameter for an optical resonator, which measures its capability of “trapping” the energy of light. Generally, it is defined as [3-14]:

$$Q = \omega \frac{\text{field energy stored by resonator}}{\text{power dissipated by resonator}} \quad (3.12)$$

In our case:

$$Q = \frac{\lambda_0}{FWHM} \quad (3.13)$$

As we can see from Figure 3-8, the quality factor of smaller hole size has a better performance than larger one, which indicates that the cavity with a smaller diameter can effectively trapped the energy inside of it, in contrast, a larger diameter permits the optical energy flow away from the cavity. The conclusion made from Figure 3-7 provides a strong evidence that support our hypothesis about the evanescent and propagated wave.

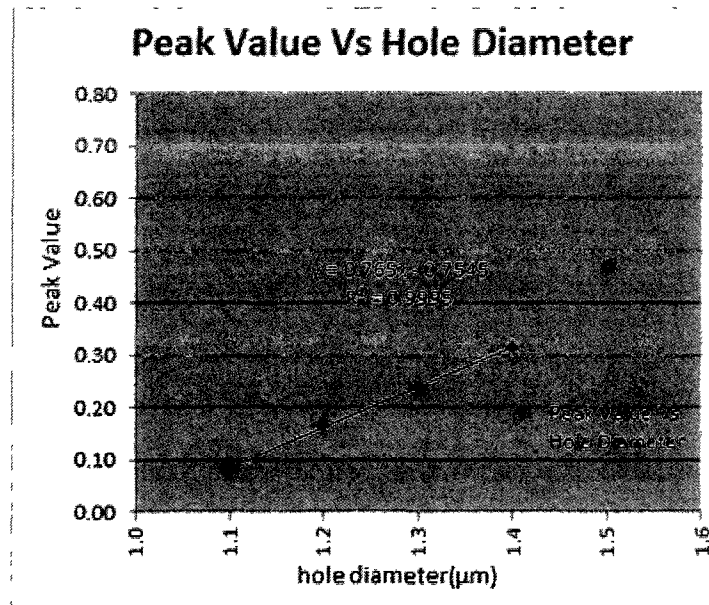


Figure 3. 6 The relationship between Peak Value and hole size.

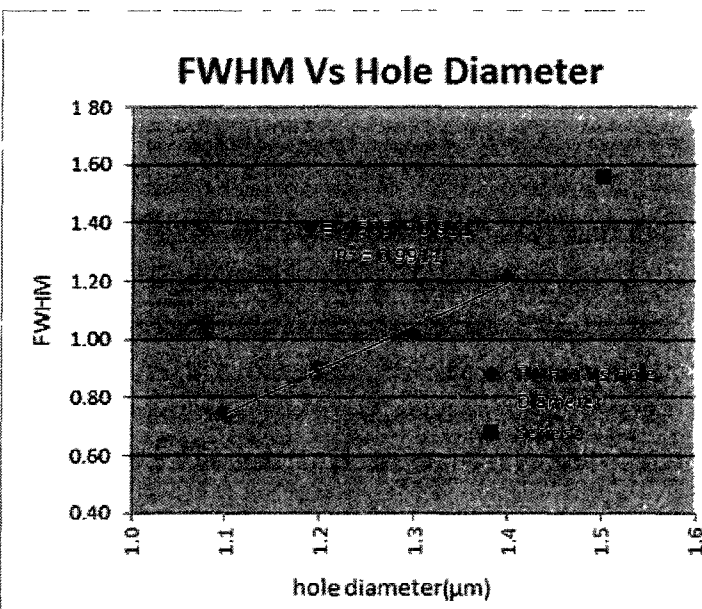


Figure 3. 7 The relationship between FWHM and hole size.

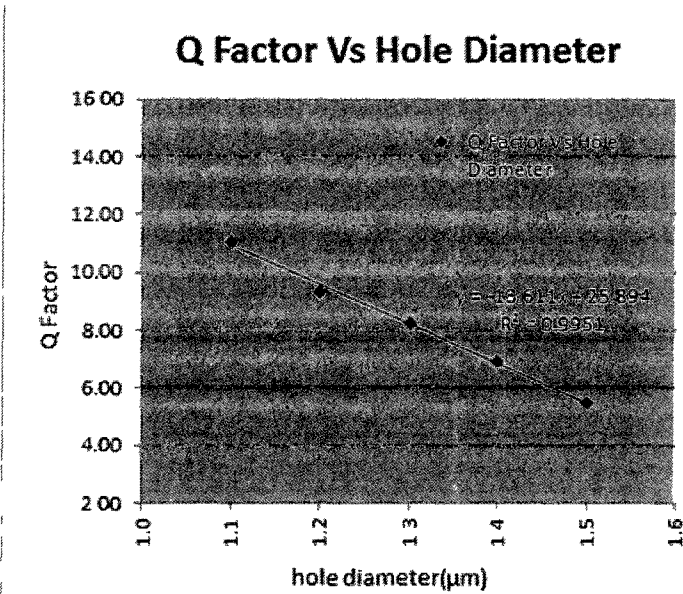


Figure 3. 8 The relationship between Q factor and hole size.

3.2 Surface Plasmon Enhanced QDIPs

3.2.1 Integration of 2DMHA on QDIPs and the Photocurrent Enhancement

After Rapid Thermal Annealing, standard QDIPs was ready for further processing. As described in Chapter3, QDIP array experienced the ultrasonic cleaning, oxygen plasma stripping, spin-coating, soft baking, exposing, developing, metal deposition and lift-off.

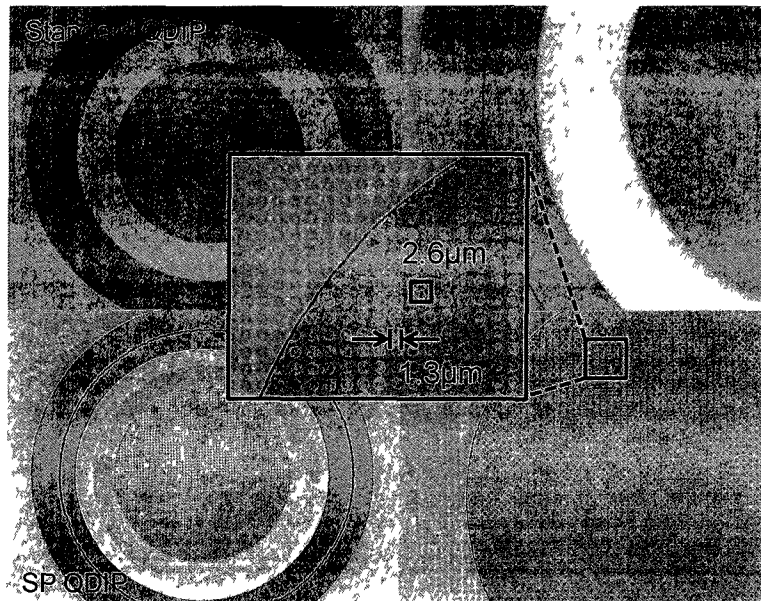


Figure 3. 9 Comparison between standard QDIP and SP integrated QDIP.

Figure 3-9 shows the comparison between standard QDIP and the SPs integrated QDIP. The period of the hole array is $2.6\mu\text{m}$, hole size is $1.3\mu\text{m}$, the thickness of the Au film is 30nm. After the fabrication, we mounted the sample in the chamber and tested the spectrum response at 77K. The FTIR result is demonstrated as below, in Figure 3-10, the black curve stands for a regular mesa, the red curve is the response of mesa integrated with 2DMHA on top. For sample UML0285, regular mesa gathered infrared signal from $3.5\mu\text{m}$ to $9.5\mu\text{m}$, with the central picking wavelength ranged from $7.0\mu\text{m}$ to $9.0\mu\text{m}$. After

applied the 2DMHA, spectrum response have a 3.1 times enhancement (which is the ratio of the black curve over the red curve), located at $8.6\mu\text{m}$, and the peaks larger than $9.5\mu\text{m}$ might be result from the noise fluctuation. Figure 3.12 ~Figure 3.16 show the performance enhancement on Photocurrent, Gain, Responsivity, Detectivity and Quantum Efficiency.

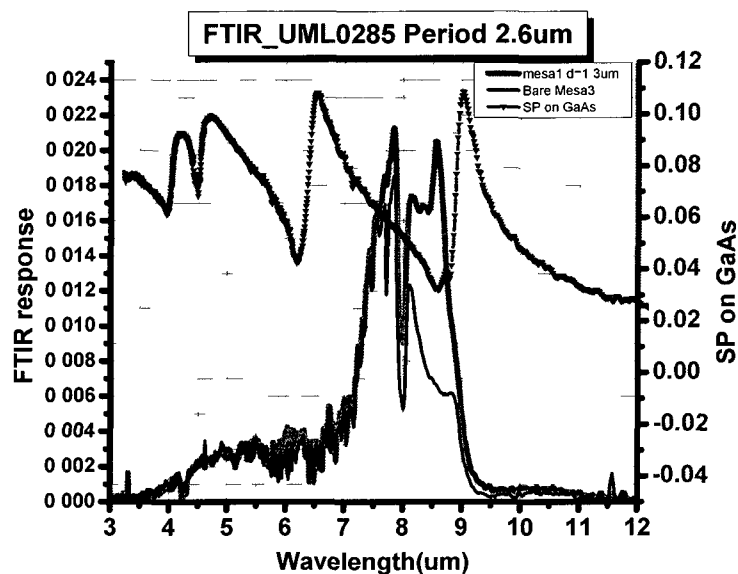


Figure 3. 10 FTIR response of regular QDIP and Plasmonic integrated QDIP with period 2.6um.

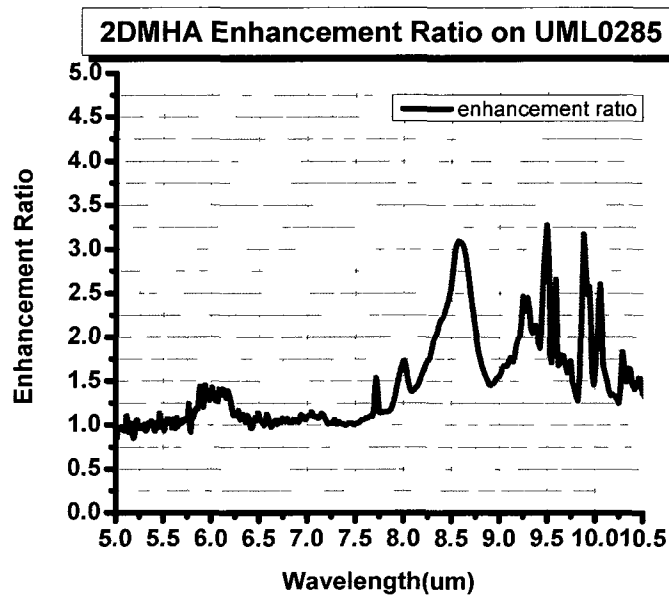


Figure 3. 11 Enhancement Ratio for $2.6\mu\text{m}$ period 2DMHA on UML0285.

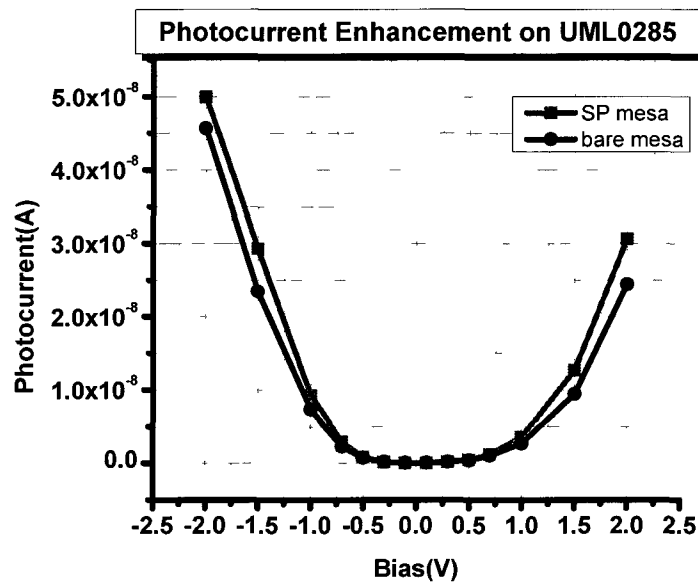


Figure 3. 12 Photocurrent Enhancement for $2.6\mu\text{m}$ period 2DMHA on UML0285.

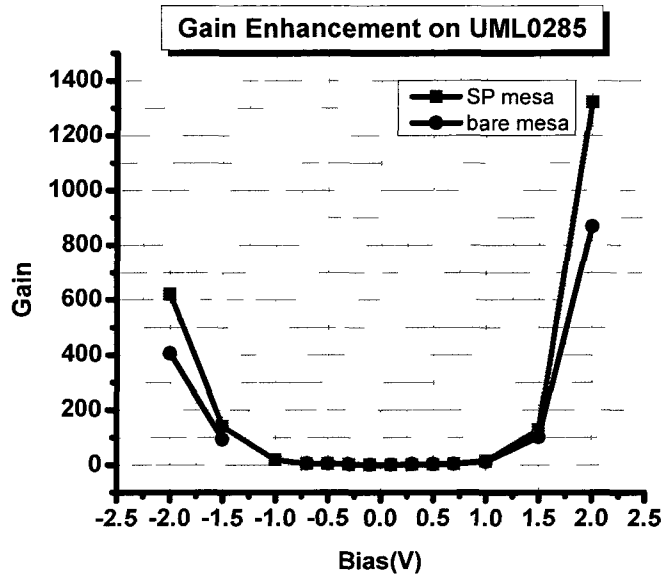


Figure 3. 13 Gain Enhancement for $2.6\mu\text{m}$ period 2DMHA on UML0285.

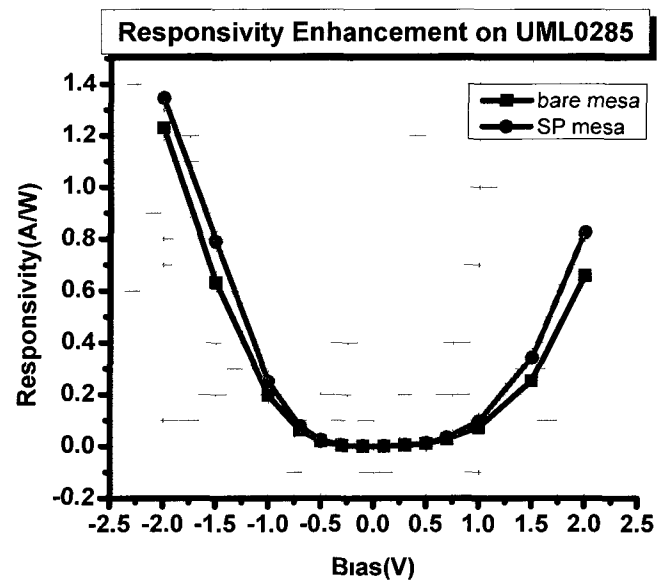


Figure 3. 14 Responsivity Enhancement for $2.6\mu\text{m}$ period 2DMHA on UML0285.

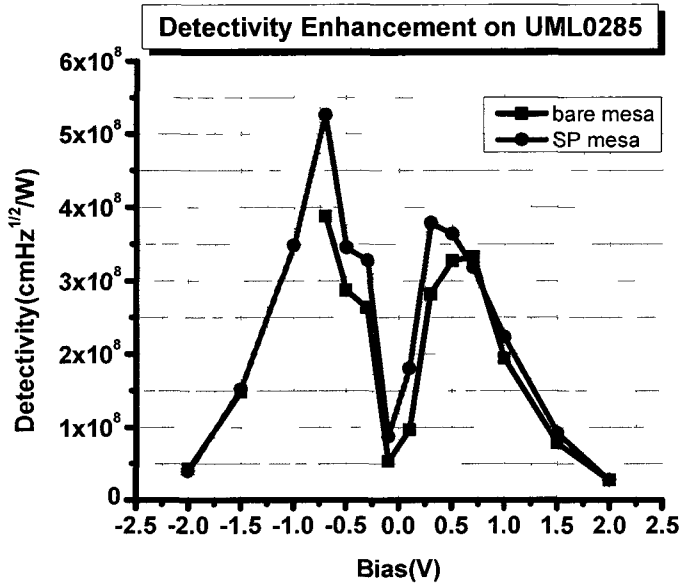


Figure 3. 15 Detectivity Enhancement for $2.6\mu\text{m}$ period 2DMHA on UML0285.

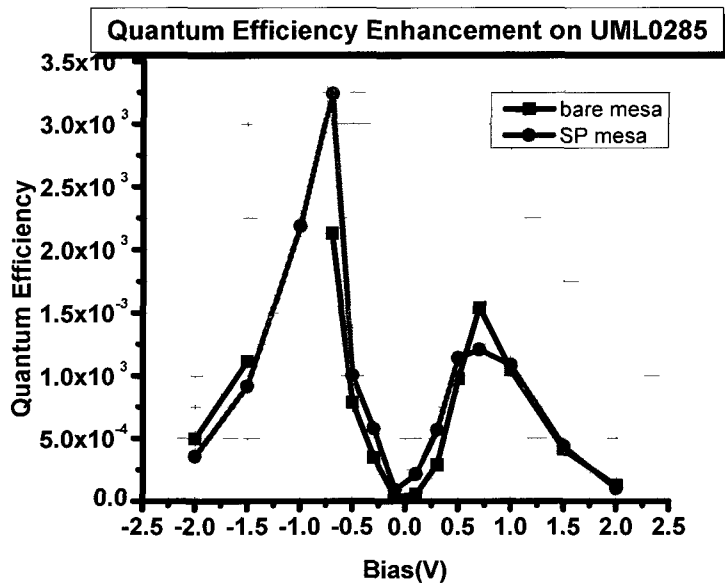


Figure 3. 16 Quantum Efficiency Enhancement for $2.6\mu\text{m}$ period 2DMHA on UML0285.

3.2.2 Enhancement Peak Shifting and Its Dependence on Lattice Constant

In Figure 3.3, as we discussed before, SPs resonance wavelength is highly depends on the lattice constant a , and for the lattice constant $a = 2.6\mu\text{m}$, the Fano dip is

around $8.4\mu\text{m}$, which matches with our experimental result, since the dip position indicates that the incident optical field with the energy at that specific wavelength has been trapped by the array pattern. Based on the previous theoretical analysis and experiment results, we can make the speculation that by changing the lattice constant, the enhanced wavelength can be tuned to the particular range that we are interested in. Designed to be sensitive to a certain wavelength, our detectors can benefit a lot from this technology, as it will improve the performance right at the wavelength we want. To further prove the assumption, we then made 2DMHA with lattice constant of $2.4\mu\text{m}$ on sample UML0287, $2.8\mu\text{m}$ and $3.0\mu\text{m}$ on sample UML0282.

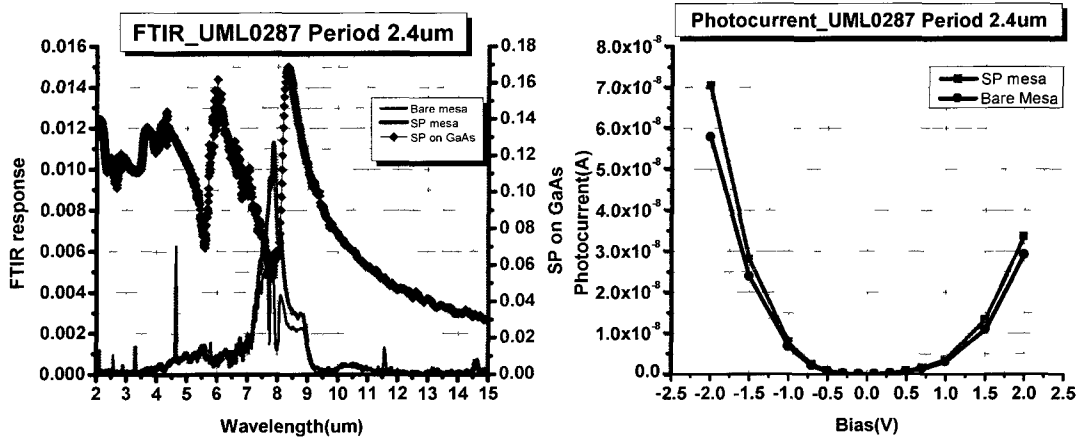


Figure 3. 17 FTIR and Photocurrent enhancement for period $2.4\mu\text{m}$.

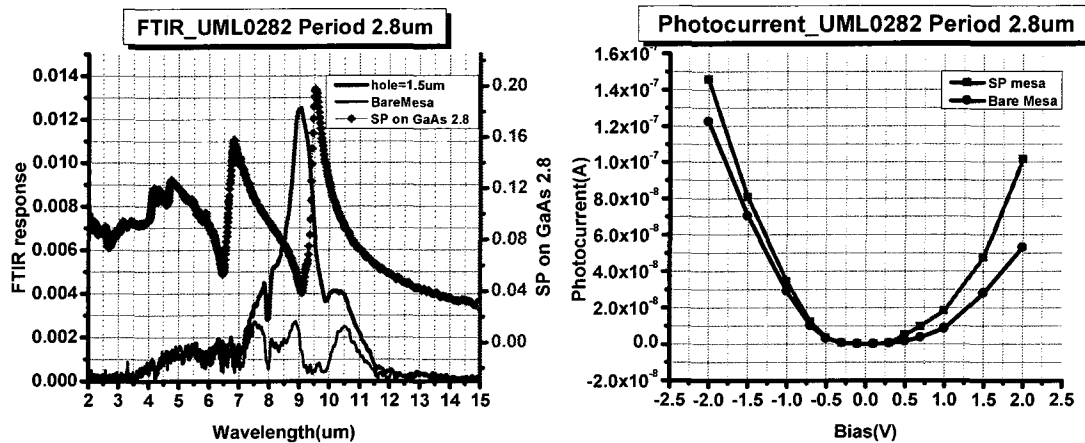


Figure 3. 18 FTIR and Photocurrent enhancement for period $2.8\mu\text{m}$.

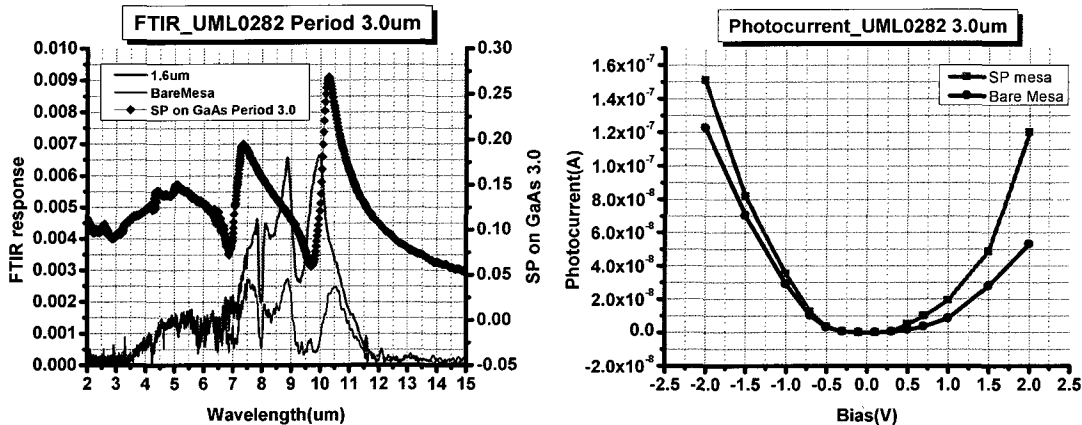


Figure 3. 19 FTIR and Photocurrent enhancement for period $3.0\mu\text{m}$.

As we can see from Figure 3.17, Figure 3.18, Figure 3.19, the enhancement peaks are located at the Fano dips where energy supposed to be trapped by the metal hole array. Table 3-2 listed the exact enhancement peak position and the enhancement ratio for arrays with different lattice constants.

Period(um)	Hole Size(um)	Enhancement Peak(um)	Enhancement Ratio
2.4	1.2	7.9	10.69
2.6	1.3	8.6	3.09
2.8	1.5	9.0	5.52
3.0	1.6	9.7	9.80

Table 3. 1 Enhancement peak and ratio with different lattice constant.

3.2.3 Enhancement Ratio Variation and Its Dependence on Filling Factor

To explore the impact of filling factor on the enhancement ratio, we designed the patterns of mask with different hole size and keep the lattice constant unchanged, then integrated them on our detectors. Figure 3.20, Figure 3.21 shows SP integrated QDIP with different d .

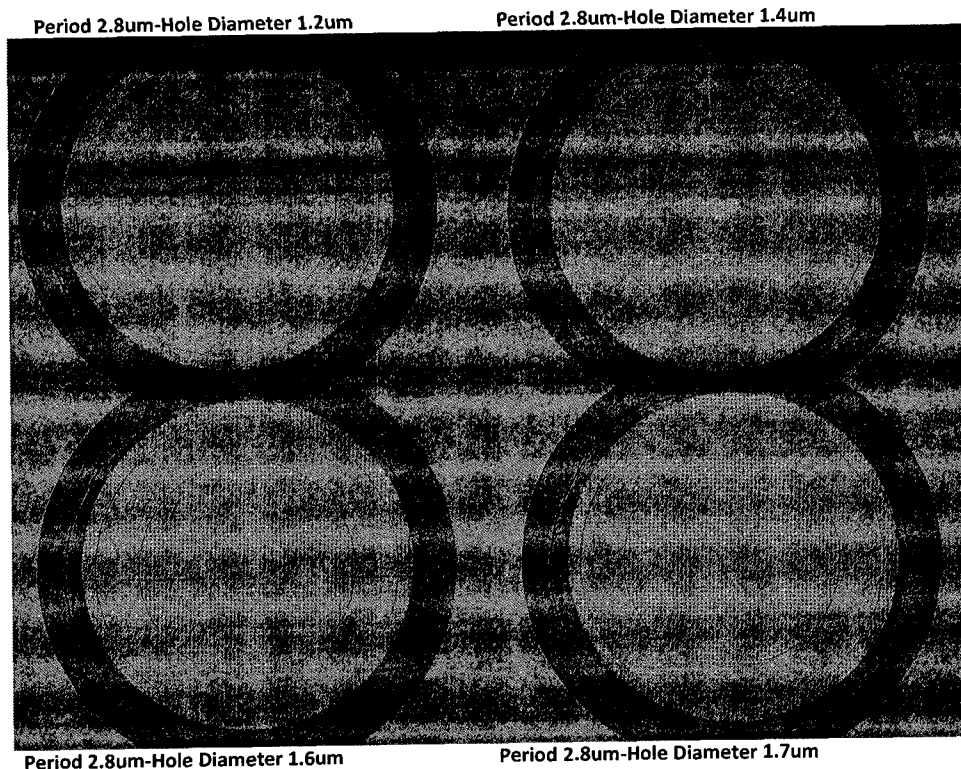


Figure 3. 20 Regular QDIPs integrated with 2DMHA of different filling factor 20X.

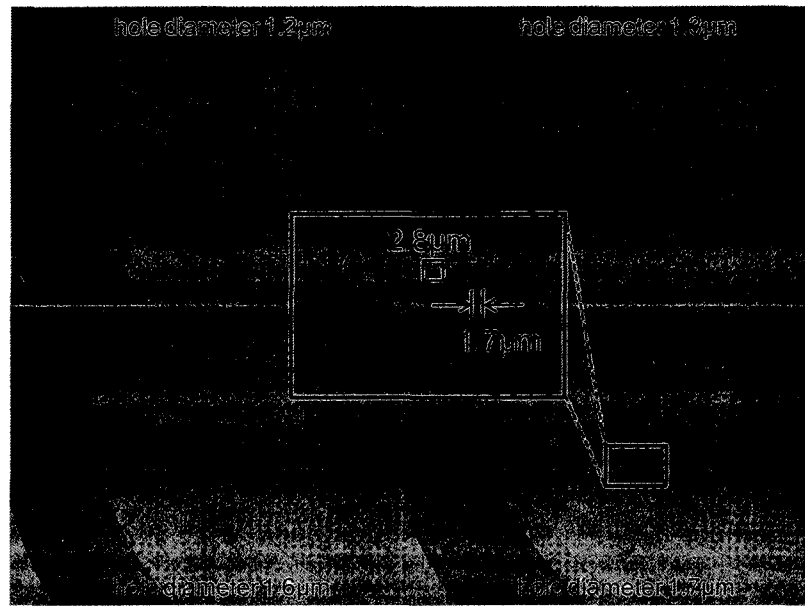


Figure 3. 21Regular QDIPs integrated with 2DMHA of different filling factor 50X.

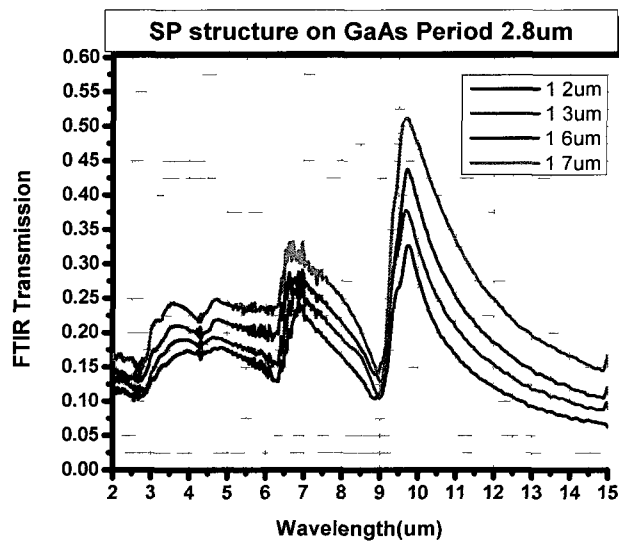


Figure 3. 22 Transmission of SP on GaAs Period 2.8um.

Figure 3.22 shows the FTIR transmission spectral response of the 2DMHA with different hole size on GaAs wafer. The lattice constant of the array is 2.8um, according to the curves, two series of transmission peaks exist on the graph, corresponding to the wavelength a 9.7μm and 6.7μm respectively. Those peaks located exactly at the SP

resonant wavelengths ((1,0), (0,1), (1,1) mode). The transmission efficiency increases along with the enlargement of the hole diameter.

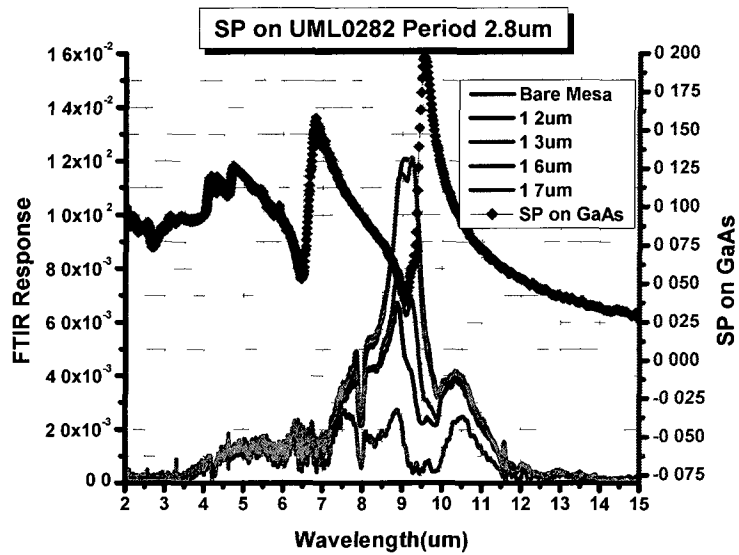


Figure 3.23 FTIR spectral response of the mesa integrated with 2DMHA of different filling factors.

Figure 3.23 shows the photocurrent enhancement of the mesas integrated with 2DMHA of different filling factors. As discussed before, the enhancement peak occurred at the same position of the Fano dip in the transmission spectrum on bare GaAs. It should be noticed that the enhancement ratio keep growing when the diameter increases from 1.2um to 1.6um, however, for the 1.7um, the trend stopped, which is different from the behavior of transmission through bare GaAs. To understand this phenomenon, we should remind that the Fano-type interference between a continuous state and a discrete state of the optical field is the working mechanism of the plasmonic enhancement in near field. The discrete state here is the plasmonic wave under resonance, the continuous state is the radiative damping of the surface plasmons through the holes. As the lattice constant remains the same in all the arrays we considered above, the contribution from the discrete

state assume to be equal in each sample. Therefore, the only reason that leads to the variation of the enhancement should be attribute to the continuous state, which is the interaction between the SP and the holes.

In order to explore the mechanism that support this phenomenon, let us assume each hole perforated on the metal film can be characterized as a micro cylindrical waveguide.

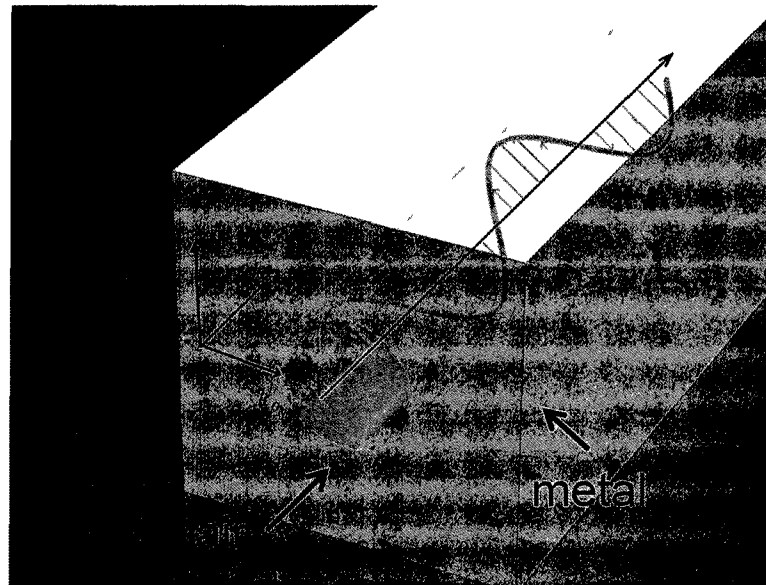


Figure 3. 24 Cylindrical waveguide in the metal film

According to Maxwell equation [20]:

$$\nabla \times H = i\omega\epsilon_0 n^2 E \quad (3.14a)$$

$$\nabla \times E = -i\omega\mu H \quad (3.14b)$$

By eliminating H or E , we obtained the Helmholtz equation:

$$\nabla^2 E + \omega^2 \epsilon_0 \mu n^2 E = 0 \quad (3.15a)$$

$$\nabla^2 H + \omega^2 \epsilon_0 \mu n^2 H = 0 \quad (3.15b)$$

For the cylindrical waveguide, the TE mode can be transformed into:

$$-i\omega\mu H_z = -\frac{1}{r} \frac{\partial}{\partial\varphi} E_r + \frac{1}{r} \frac{\partial}{\partial r} (r E_\varphi) \quad (3.16a)$$

$$i\omega\epsilon E_r = \frac{1}{r} \frac{\partial}{\partial\varphi} H_z + i\beta H_\varphi \quad (3.16b)$$

$$i\omega\epsilon E_\varphi = -\frac{\partial}{\partial r} H_z - i\beta H_r \quad (3.16c)$$

H_z should satisfy the Helmholtz equation in the cylindrical form:

$$\left[\frac{\partial^2}{\partial r^2} + \frac{1}{r} \frac{\partial}{\partial r} + \frac{1}{r^2} \frac{\partial^2}{\partial\varphi^2} + (k_0^2 - k_z^2) \right] H_z = 0 \quad (3.17)$$

Using the separation variable method:

$$H_z = R(r)\Phi(\varphi)e^{ik_z z} \quad (3.18)$$

Where:

$$\Phi(\varphi) = \exp(\pm il\varphi) \quad (3.19a)$$

$$\frac{\partial^2 R}{\partial r^2} + \frac{1}{r} \frac{\partial R}{\partial r} + \left(k_0^2 - k_z^2 - \frac{l^2}{r^2} \right) R = 0 \quad (3.19b)$$

Equation (3.19b) matches the form of Bessel Function, its solution should be:

$$R(r) = C_l J_l(\sqrt{k_0^2 - k_z^2} r) \quad (3.20)$$

Thus:

$$H_z = J_l(\sqrt{k_0^2 - k_z^2} r) \exp(\pm il\varphi) e^{ik_z z} \quad (3.21)$$

The boundary condition at $r = a$ requires that the tangential component of E be zero, (in conductor, tangential component of E always equal to zero), $E_\varphi = 0$.

Which means:

$$\left[\frac{\partial H_z}{\partial r} \right]_{\rho=a} = 0 \quad (3.22)$$

In another word:

$$J_l' \left(\sqrt{k_0^2 - k_z^2} a \right) \exp(\pm il\varphi) e^{ik_z z} = 0 \quad (3.23)$$

$$J_l' \left(\sqrt{k_0^2 - k_z^2} a \right) = 0 \quad (3.24)$$

k	$J'_0(x)$	$J'_1(x)$	$J'_2(x)$	$J'_3(x)$	$J'_4(x)$	$J'_5(x)$
1	3.8317	1.8412	3.0542	4.2012	5.3175	6.4156
2	7.0156	5.3314	6.7061	8.0152	9.2824	10.5199
3	10.1735	8.5363	9.9695	11.3459	12.6819	13.9872
4	13.3237	11.706	13.1704	14.5858	15.9641	17.3128
5	16.4706	14.8636	16.3475	17.7887	19.196	20.5755

Table 3. 2 First few roots for differential of first Bessel Function

Considering the lowest order for simplicity, for LP₀₁ mode, the corresponding

solution is $J'_0(U) = 0$, $x = \sqrt{k_0^2 - k_z^2} a = k_\rho a = 3.83$.

In our case, at the air-metal interface, $n_1 = 1$, $k_0 = \frac{2\pi}{\lambda_{SPP}} = \frac{2\pi}{8.97} = \sqrt{k_\rho^2 + k_z^2}$, $\beta = k_z$,

then:

$$k_\rho = \sqrt{\left(\frac{2\pi}{8.97}\right)^2 - k_z^2} = \frac{3.83}{a} \quad (3.25a)$$

$$k_z = \sqrt{\left(\frac{2\pi}{8.97}\right)^2 - \left(\frac{3.83}{a}\right)^2} \quad (3.25b)$$

diameter	k0	kp	kz
1.2	0.70047	3.19167	i3.11385
1.3		2.94615	i2.86167
1.4		2.73571	i2.64452
1.6		2.39375	i2.28897
1.7		2.25294	i2.14128

Table 3. 3 Relationship between d and kz in air.

Obviously, $k_0^2 < k_p^2$, so k_z is an imaginary number, substitute k_z into wave function:

$$\Psi(z, t) = \psi \exp [i(\omega t - k_z z)] = \psi \exp i(\omega t) \exp (-\kappa) \quad (3.26)$$

Equation (3.26) stands for an evanescent decay mode with $|k_z|^{-1}$ as the $1/e$ decay length L_d

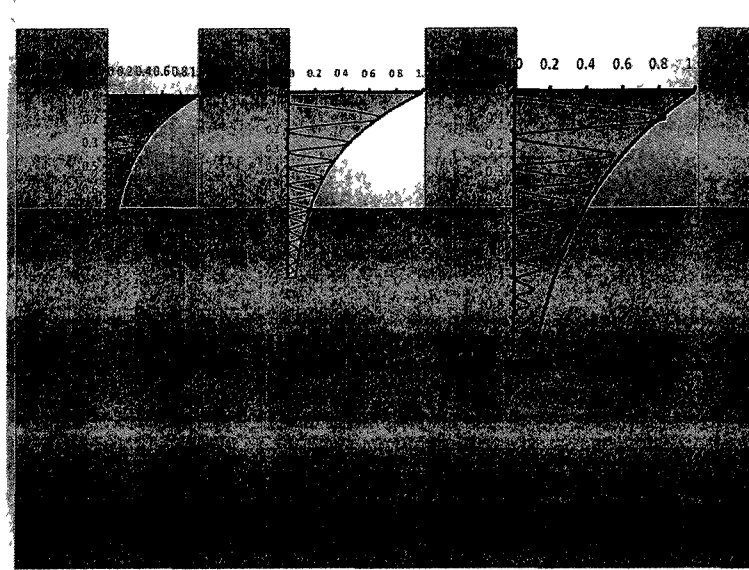


Figure 3. 25 E-field decay of different hole diameters in the air hole.

Figure 3.25 shows the decay of different hole diameters. The larger diameter correspond to longer decay length L_d , Figure 3.26 gives us a schematic view of how these E-Field spread in a QDIP.

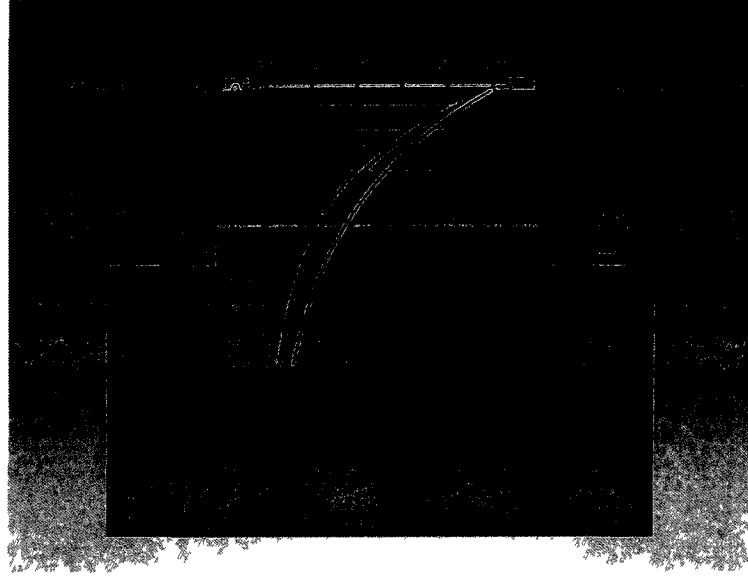


Figure 3. 26 Decay curve on the QDIP.

Figure 3.27 shows the $|k_z|$ v.s. the FWHM widths of the transmission peaks with different hole diameters. For a wave like $E = E_0 \exp(-k_z z)$, the distance for the $1/e$ amplitude is $z = 1/k_z$, the lifetime is $\tau = 1/k_z c$. Since the FWHM spectral width indicates the loss of the optical field, which should be proportional to $1/k_z$ [21], as we can tell from the figure, a good linearity is obtained for FWHM and k_z . It is confirmed that the evanescent modes are the dominating damping mechanism for the SPWs.

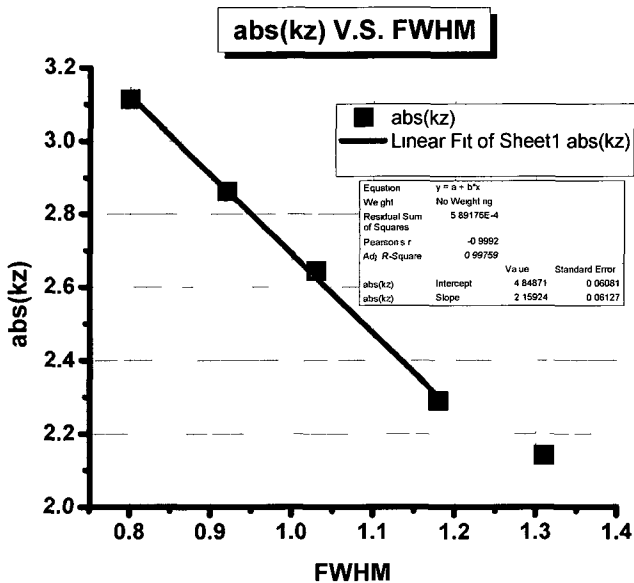


Figure 3.27 FWHM widths different hole diameters.

At the lower plane, the metal-dielectric interface, the radical wave vector will remain unchanged, $k_\rho = \frac{3.83}{a}$, while k_0 should be modified as $k_0 = \frac{2\pi n}{\lambda_{SPP}}$, where n is the refractive index of the semiconductor, in our case, it's the GaAs at $9.0\mu\text{m}$ ($n_{GaAs} = 3.31$, $\lambda_0 = 9.0\mu\text{m}$).

diameter	k0	kx	kz
1.2	2.31855	3.19167	i2.19341
1.3		2.94615	i1.81773
1.4		2.73571	i1.45205
1.6		2.39375	i0.59529
1.7		2.25294	0.54766

Table 3.4 Relationship between d and kz in GaAs.

According to table 3.4, in the GaAs, the E-field shows the behavior as an evanescent wave when the diameter is equal or smaller than $1.6\mu\text{m}$, but when it comes to $1.7\mu\text{m}$, the wave vector along vertical direction turns to real number, which means that the E-field changes to propagating mode. See figure 3.28 below.



Figure 3. 28 E-field distribution inside of GaAs.

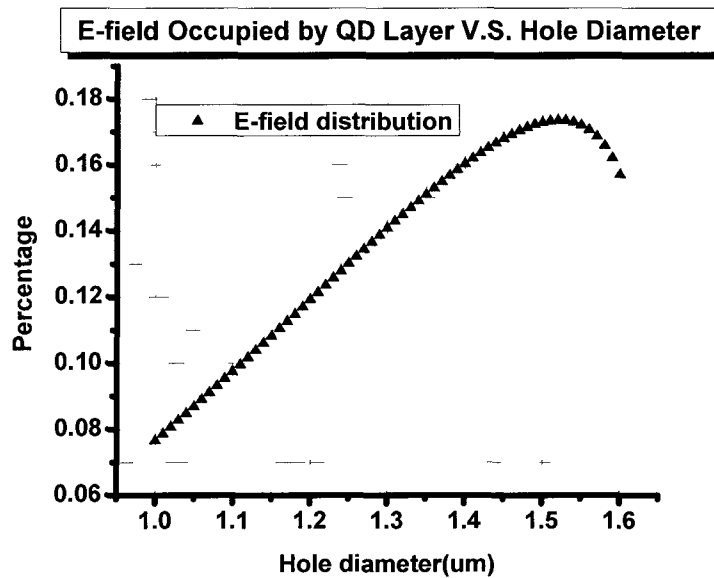


Figure 3. 29 Percentage of E occupied by QDs layer through different hole diameters.

For the sample UML0282, the 10 layer QDs were distributed within the range of $0.250\mu\text{m}$ to $0.826\mu\text{m}$ away from the top. In order to examine how much of the electric field that involved to interacts with the active layer, we calculate the integration of $\exp(-k_z z)$ over the range of $(0.250, 0.826)$, and normalized to the total integration from

0 to $+\infty$. Figure 3.29 shows the percentage of electric field that distributed in the active region. As shown in the curve, along with the enlargement of the hole diameter ($1.1\mu\text{m}$ - $1.6\mu\text{m}$), the percentage of energy that occupied by the QDs layer keep increasing, while when the diameter reaches $1.7\mu\text{m}$, the k_z becomes a real number, and the mode starts to radiate. For the radiation modes, the intensity of Electric-field will not be tuned too much, this partially explains why the FTIR enhancement ratios of $1.6\mu\text{m}$ and $1.7\mu\text{m}$ doesn't show any big change, which might be attribute to the enhancement saturation. In order to further prove this phenomenon, we integrated the standard QDIPs with 2DMHA of different filling factors and test the performance as we did on UML0282. Figure 3-26 shows the calculation E-field distribution of period $2.6\mu\text{m}$ series for a 10 layer device. The red dot stands for the peak value of FTIR response from QDIP integrated with 2DMHA of different hole diameters. Figure 3.31, Figure 3.32 show the FTIR spectral response of UML0287 integrated with 2DMHA of 2.6 series.

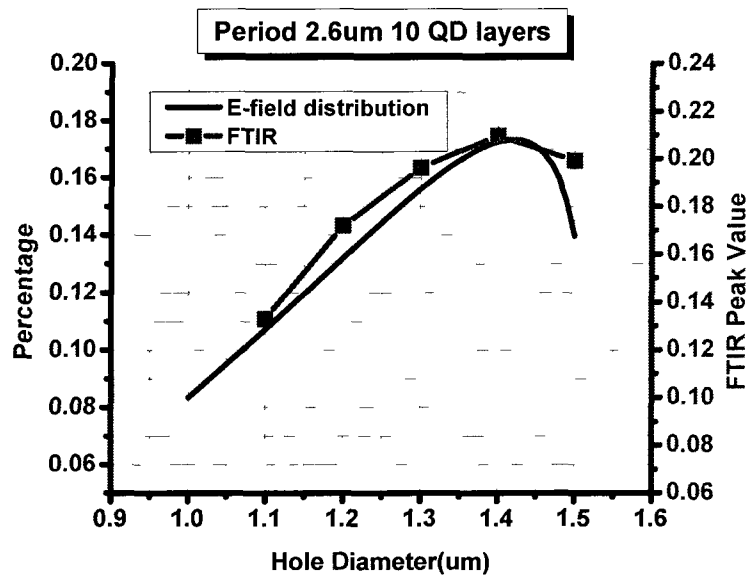


Figure 3. 30 Matlab calculation for 2.6 series on 10 layer QDs.

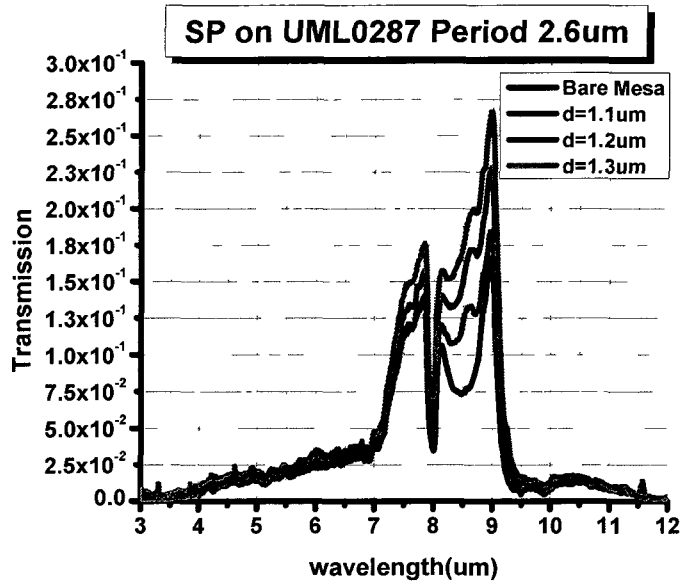


Figure 3.31 FTIR response of $1.1\mu\text{m}$, $1.2\mu\text{m}$ and $1.3\mu\text{m}$ on UML0287.

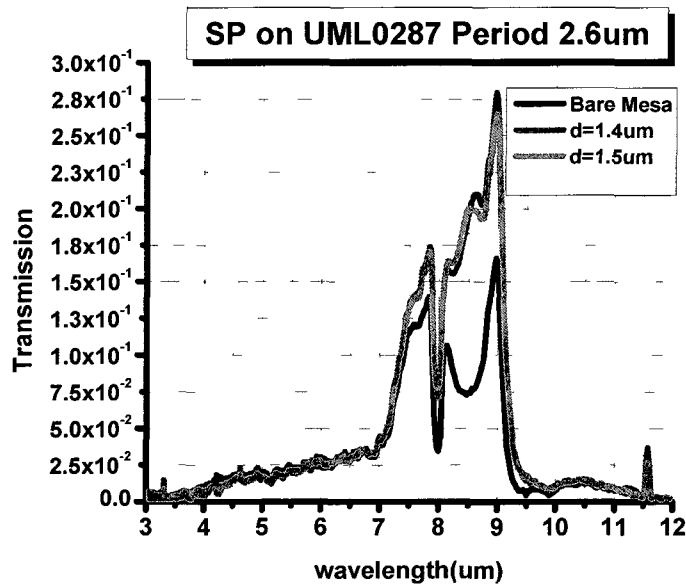


Figure 3.32 FTIR response of $1.4\mu\text{m}$ and $1.5\mu\text{m}$ on UML0287.

Figure 3.33 shows the calculation E-field distribution of period $2.8\mu\text{m}$ series for a 20 layer device (for 20 layer device, the dots layer starts from $0.25\mu\text{m}$ to $1.6\mu\text{m}$). Again the red dots are peak values of FTIR response. Figure 3.34 shows the FTIR spectral response of UML2461 integrated with 2DMHA of different filling factors.

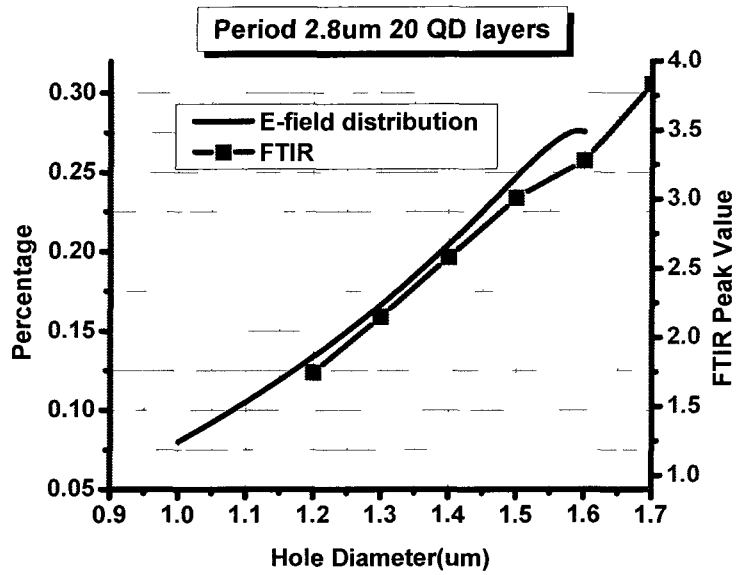


Figure 3. 33 Matlab calculation for 2.8 series on 20 layer QDs

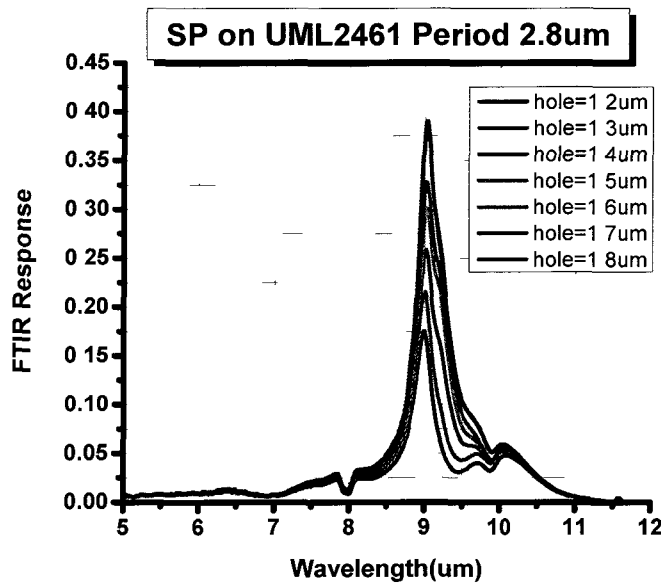


Figure 3. 34 FTIR response of 1.2μm-1.8μm on UML2461.

According to the experimental results, we realize that the photocurrent enhancements for different filling factors fit the trend that predicted by our analysis. And the evanescent damping mode did play an indispensable role for the near field transmission enhancement.

3.2.4 Performance Enhancement for Different Filling Factors

To have a complete evaluation on the SPP enhanced QDIPs, we collect the data and plot the curves of Photocurrent, Responsivity and Detectivity in the following series of Figures.

First of all, Figure 3.35~Figure 3.40 are the performance enhancement of UML0287. Noticing that each parameter is divided into two part, in the first part, the enhancement ratio keep increasing along with the enlargement of the hole diameter, which is leaded by the relationship between decay of the E-field and the hole diameters (discussed before, larger d , smaller k_z , longer τ); in the second part, the enhancement ratio tends to remain the same, which is due to the saturation of the enhancement, since the mode turns to the radiation mode in the GaAs when the diameter large enough to make k_z become a real number.

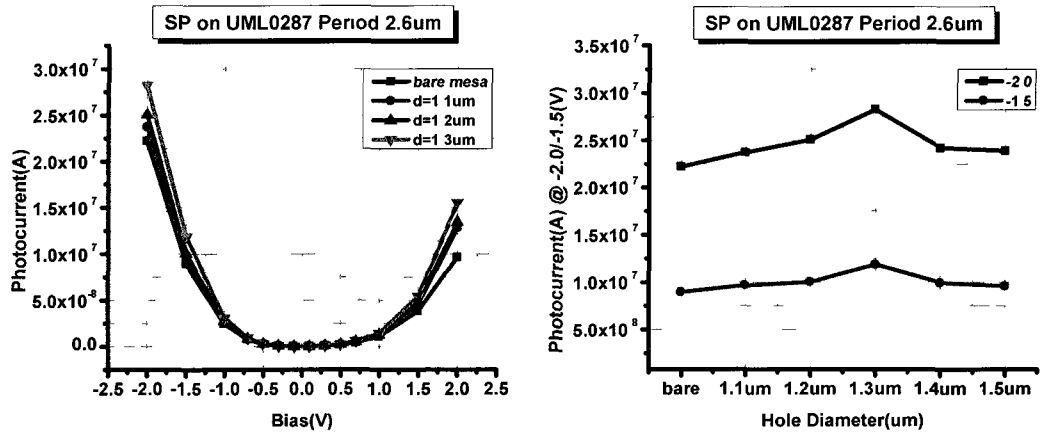


Figure 3. 35 Photocurrent of UML0287 with different filling factors (bare&1.1um-1.3um).

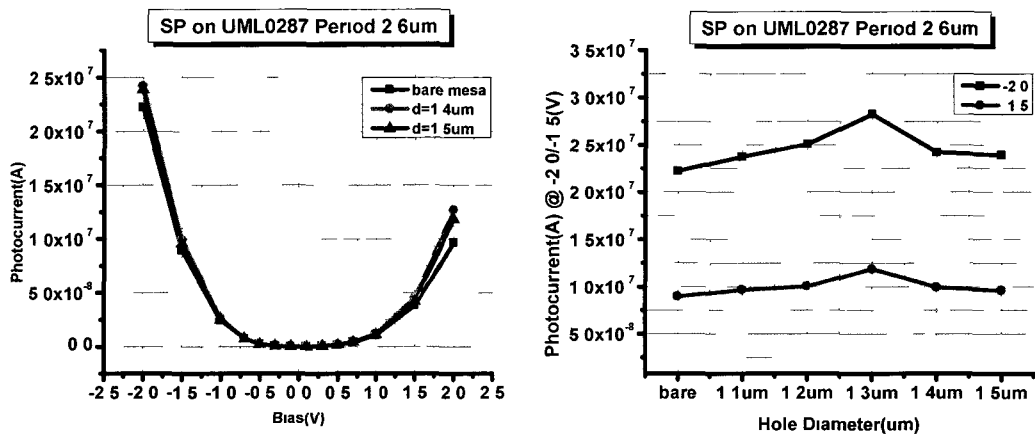


Figure 3.36 Photocurrent of UML0287 with different filling factors (bare&1.4um, 1.5um).

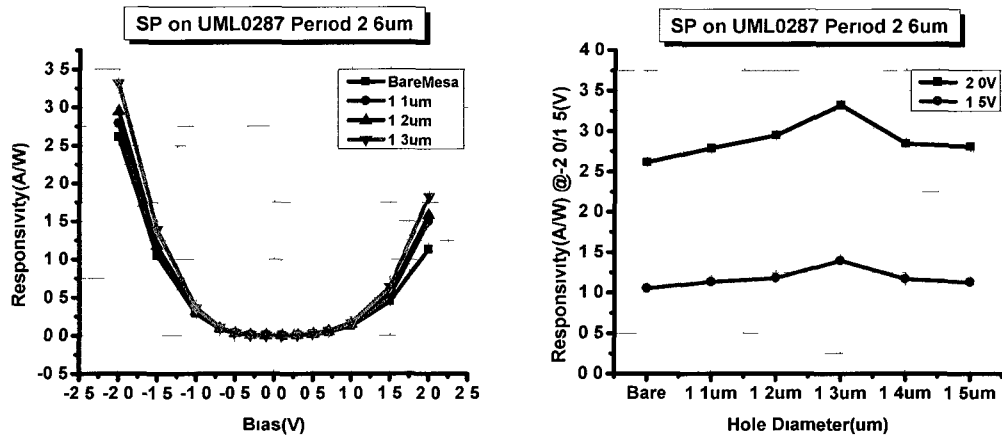


Figure 3.37 Responsivity of UML0287 with different filling factors (bare&1.1um-1.3um).

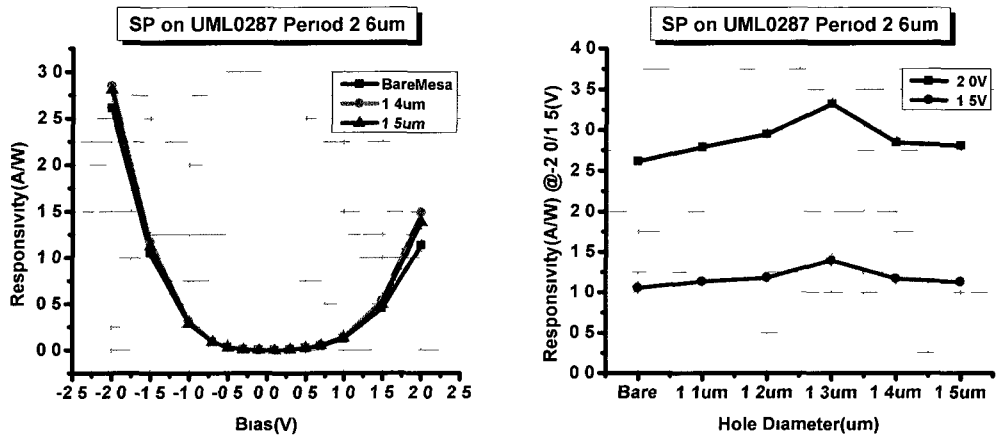


Figure 3. 38 Responsivity of UML0287 with different filling factors (bare&1 4um, 1.5um)

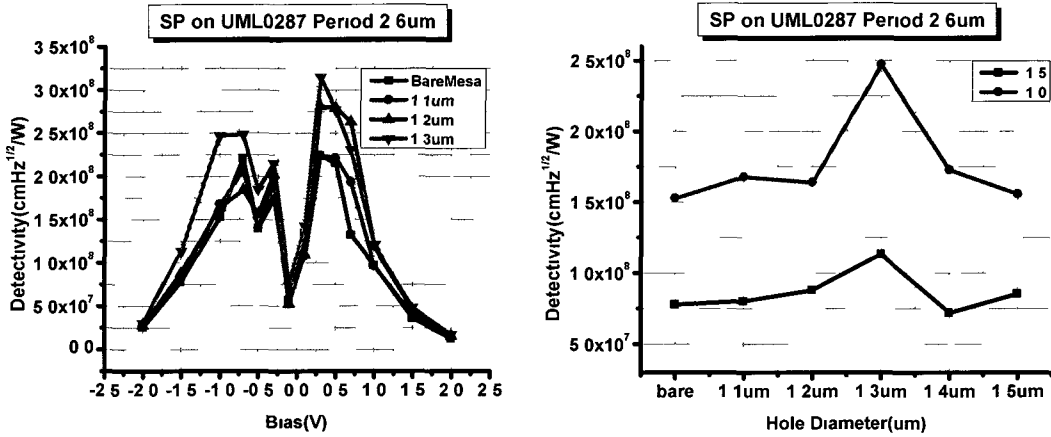


Figure 3. 39 Detectivity of UML0287 with different filling factors (bare&1 1um-1 3um)

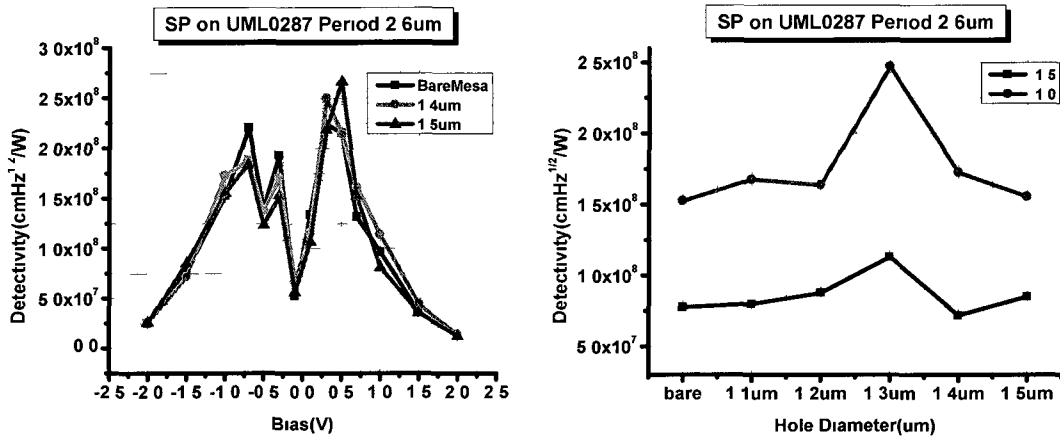


Figure 3. 40 Detectivity of UML0287 with different filling factors (bare&1 4um, 1.5um).

As for the second part, Figure 3.41 ~ Figure 3.43 are the performance enhancement of UML2461. Different from the enhancement result from UML0287, the enhancement ratio keep increasing with the enlargement of the hole diameter. The difference from the two sample is the number of QD layers, for UML0287, the total number is 10, but for UML2461, the number increases to 20. Consequently, the thickness

of active region is quite different (UML0287 is from $0.25\mu\text{m}$ to $0.826\mu\text{m}$, UML2461 is from $0.25\mu\text{m}$ to $1.60\mu\text{m}$).

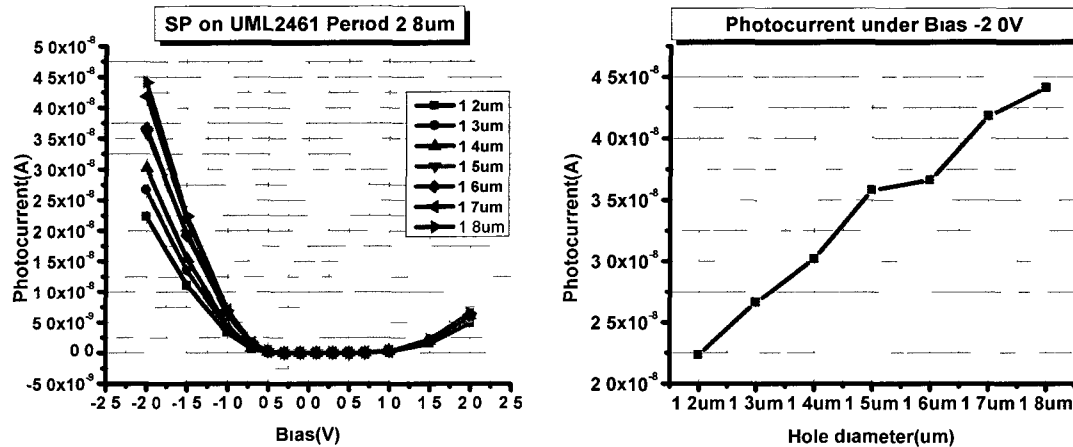


Figure 3.41 Photocurrent enhancement on UML2461 with different filling factors

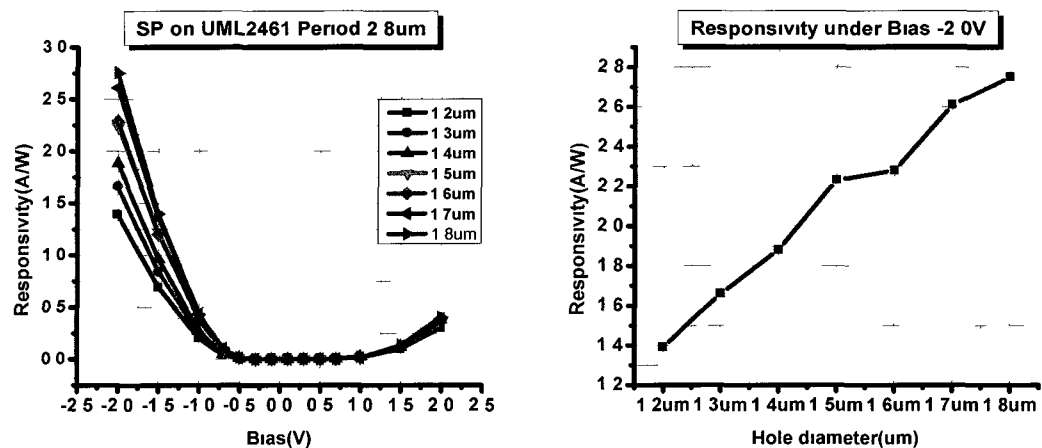


Figure 3.42 Responsivity enhancement on UML2461 with different filling factors.

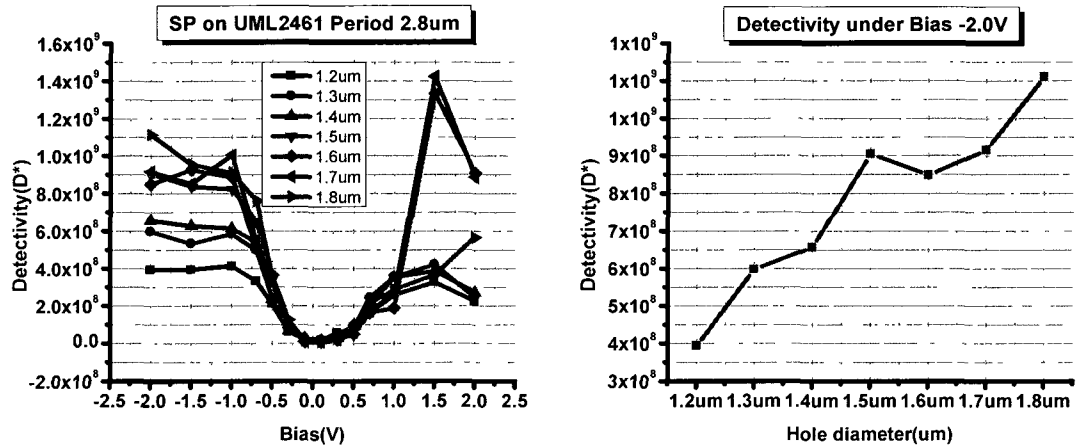


Figure 3. 43 Detectivity enhancement on UML2461 with different filling factors.

IV. CONCLUSION AND FUTURE WORK

4.1 Conclusion

In summary, a metallic two-dimensional subwavelength hole array structure is integrated on quantum dot infrared photodetector; photocurrent enhancement has been observed, the enhancement peak occurs at the plasmonic resonant wavelength, and can be tuned by manipulating the lattice constant of the hole array; enhancement ratio and its dependence on the filling factor is investigated, the impact from evanescent waveguide mode has been analyzed; by exploring the relationship between the radical wavevector and the E-field spreading along the vertical direction, a final conclusion has been claimed, that the QDIP performance improvement is closely bond to the hole diameter, which can have influence on the E-field spreading and control the amount of energy that effectively interact with the active QD layer.

4.2 Future Work

In the discussion above, we mainly talked about the cylindrical hole that drilled on the metal film, in the future, we can further developed other shape holes, such as the square one. As listed before, we obtained the Helmholtz equation:

$$\nabla^2 E + \omega^2 \epsilon_0 \mu n^2 E = 0 \quad (4.1a)$$

$$\nabla^2 H + \omega^2 \epsilon_0 \mu n^2 H = 0 \quad (4.1b)$$

For a square hole, calculation should be operated under Cartesian Coordinate, for simplicity, the electric and magnetic field can be expressed as below:

$$E(x, t) = E_0(x) \exp[i(\omega t - k_z)] \quad (4.2a)$$

$$H(x, t) = H_0(x) \exp[i(\omega t - k_z)] \quad (4.2b)$$

Substitute (4.2) into (4.1):

$$\nabla^2 E(x) + [k_0^2 n^2 - k_z^2] E(x) = 0 \quad (4.3a)$$

for TE wave,

$$\nabla^2 H(x) + [k_0^2 n^2 - k_z^2] H(x) = 0 \quad (4.3b)$$

for TM wave,

where $k_0^2 n^2 - k_z^2 = k_x^2$, and $k_0^2 n^2$ is a constant value.

Based on the previous derivation, the condition for the Plasmon mode to resonant on the surface is:

$$\gamma = \left(\frac{\omega}{c}\right) \sqrt{\frac{\varepsilon_1 \varepsilon_2}{\varepsilon_1 + \varepsilon_2}} \quad (4.4)$$

When the surface Plasmon mode propagate along the interface and hit the hole, some of the energy will couple to the cavity, in that case, the mode inside the hole matches the equation:

$$k_z^2 + k_x^2 = \gamma^2 = \left(\frac{\omega}{c}\right)^2 \frac{\varepsilon_1 \varepsilon_2}{\varepsilon_1 + \varepsilon_2} = \left(\frac{2\pi}{\Lambda}\right)^2 \quad (4.5)$$

If $\left(\frac{2\pi}{\Lambda}\right)^2 - k_x^2 = k_z^2 = \kappa^2 < 0$, then $k_z = \pm i\kappa$ (for $z > 0$, $k_z = -i\kappa$; for $z < 0$, $k_z = i\kappa$),

$$E(x) = E_0(x) \exp[i(-k_z z)] = E_0(x) \exp(-\kappa z) \quad (4.6a),$$

which indicates that the x component of E is an evanescent field along z -direction.

Oppositely, if $\left(\frac{2\pi}{\Lambda}\right)^2 - k_x^2 = k_z^2 = \beta^2 > 0$, then $k_z = \pm \beta$ (for $z > 0$, $k_z = i\beta z$; for $z < 0$, $k_z = -i\beta z$),

$$E(x) = E_0(x) \exp[i(-k_z z)] = E_0(x) \exp(-i\beta z) \quad (4.6b)$$

which proves that the surface plasmon mode coupled into the hole is able to propagate in the waveguide along z -direction.

In our case, for the lattice constant $\Lambda = 2.8\mu m$, $k_0 = \frac{2\pi}{2.8\mu m} = 2.24$

square hole array for lattice constant 2.8um			
dimension	k0	kx	kz
1.2	2.24400	2.61800	i1.34848
1.3		2.41662	i0.89694
1.4		2.24400	0.00000
1.5		2.09440	0.80562
1.6		1.96350	1.08637
1.7		1.84800	1.27296
1.8		1.74533	1.41044

Table 4-1 the wavevector k_x, k_z for different hole size.

Table 4-1 list the value of k_z corresponding to different hole dimension.

V. LITERATURE CITED

- [1] Dereniak, E. L., Boreman, G. D., “Infrared detectors and systems”, Wiley, 1996.
- [2] Neaman, D. A., “Semiconductor Physics and Devices”, McGraw-Hill Science, 2002
- [3] Campbell, J.C. Madhukar, A., “Quantum-Dot Infrared Photodetectors”, Proceedings of the IEEE, vol. 95, pp. 1815-1827, 2007.
- [4] Liu, H. C., “Quantum dot infrared photodetector”, Opto-Electron. Rev., vol. 11, pp. 1-6, 2003.
- [5] Vasinajindakaw, P., Master’s thesis, “Verification and reduction of dark current on quantum dot infrared photodetector”, Electrical and Computer Engineering Department, University of Massachusetts at Lowell, 2009.
- [6] Harrison, P., “Quantum wells, wires, and dots”, John Wiley & Sons, 2005
- [7] Rosencher, E. and Vinter, Borge., “Optoelectronics”, Cambridge University Press, 2002
- [8] Raether H., “Surface plasmons on smooth and rough surfaces and on gratings”, vol.: 111, issue: 111, Springer, 1988.
- [9] Barnes, W., Dereux, A., Ebbesen, W., “Surface plasmon subwavelength optics”, Nature, vol. 424, pp. 824-830, 2003.
- [10] Maier, S., “Plasmonics: Fundamentals and Applications”, Springer, 2007.
- [11] Ebbesen, T. W., Lezec, H. J., Ghaemi, H. F., Thio, T. and. Wolff, P. A, “Extraordinary optical transmission through sub-wavelength hole arrays”, Nature, vol. 391, pp. 667-668, 1998.
- [12] Zayats, A. V., Maradudin, A. A., Smolyaninov, I. I., “Nano-optics of surface plasmon polaritons”, Elsevier, vol. 408, pp. 131-314, 2005.
- [13] Darmanyan, S. A. and Zayats, A. V., “Light tunneling via resonant surface plasmon polariton states and the enhanced transmission of periodically nanostructured metal films: An analytical study”, Phys. Rev. B, vol. 67, pp. 035424, 2003.
- [14] Degirona, A., Lezeca, H. J., Yamamoto, N. Ebbesen, T. W., “Optical transmission properties of a single subwavelength aperture in a real metal”, Opt. Commun., vol. 239, pp. 61-66, 2004
- [15] Degiron, A. and Ebbesen, T. W, “The role of localized surface plasmon modes in the enhanced transmission of periodic subwavelength apertures”, J. Opt. A: Pure Appl. Opt, vol. 7, pp. S90-S96, 2005.

- [16] Ghaemi, H. F. Thio, T. Grupp, D. E. Ebbesen, T. W. Lezec, H. J., "Surface plasmons enhance optical transmission through subwavelength holes", Phys. Rev. B, vol. 58; pp. 6779-6782, 1998.
- [17] Wasserman, D., Shaner, E. A. and Cederberg, J. G., "Midinfrared doping-tunable extraordinary transmission from sub-wavelength Gratings", Appl. Phys. Lett. vol. 90, pp. 191102, 2007.
- [18] Passmore, B. S., Allen, D. G., Vangala, S. R., Goodhue, W. D., Wasserman, D. and Shaner, E. A., "Mid-infrared doping tunable transmission through subwavelength metal hole arrays on InSb", Opt. Express, Vol. 17, Issue 12, pp. 10223-10230, 2009.
- [19] J. Vaillancourt, Master's thesis 'A Multispectral Quantum dot infrared photodetector', Electrical and Computer Engineering Department, University of Massachusetts at Lowell, November 2007.
- [20] Yariv, A., Yeh, P., "Photonics: optical electronics in modern communications", Oxford, 2007.
- [21] Martin-Moreno, L., Garcia-Vidal, F. J., Lezee, H. J., Pellerin, K. M.; Thio, T., Pendry, J. B., Ebbesen, T. W., "Theory of Extraordinary Optical Transmission through Subwavelength Hole Arrays", Phys. Rev. Lett., vol. 86; pages 1114-1117, 2001.
- [22] Bethe, H. A., "Theory of Diffraction by Small Holes", Phys. Rev., vol. 66, pp. 163-182, 1944